GEOCHEMICAL IMPLICATIONS OF GYPSUM ADDITION TO OIL SANDS FLUID FINE TAILINGS: LABORATORY BATCH AND COLUMN EXPERIMENTS

A Thesis Submitted to the
College of Graduate and Postdoctoral Studies
In Partial Fulfillment of the Requirements
For the Degree of Master of Science
In the Department of Geological Sciences
University of Saskatchewan
Saskatoon

By

MATTEA LORELLE COWELL

PERMISSION TO USE

In presenting this thesis in partial fulfillment of the requirement of a Postgraduate degree from the University of Saskatchewan, I agree that the Libraries of this University may make it freely available for inspection. I further agree that permission for copying of this thesis in any manner, in whole or in part, for scholarly purposes may be granted by the professor or professors who supervised my thesis work or, in their absence, by the Head of the Department of Geological Sciences or the Dean of the College of Graduate and Postdoctoral Studies. It is understood that any copying, publication or use of this thesis or parts thereof for financial gain shall not be allowed without my written permission. It is also understood that due recognition shall be given to me and to the University of Saskatchewan in any scholarly use which may be made of any material in my thesis.

Requests for permission to copy or to make other uses of materials in this thesis in whole or part should be addressed to:

Head
Department of Geological Sciences
University of Saskatchewan
114 Geology Building, 114 Science Place
Saskatoon, Saskatchewan S7N 5E2
Canada

Dean
College of Graduate and Postdoctoral Studies
University of Saskatchewan
116 Thorvaldson Building, 110 Science Place
Saskatoon, Saskatchewan S7N 5C9
Canada

ABSTRACT

Large inventories of tailings in the Alberta Oil Sands have created the need for technologies that can accelerate dewatering of fluid tailings; however, knowledge of long-term implications from these technologies is limited. This research was split into two studies, examining: 1) temporal changes in porewater chemistry and gas production in gypsum-amended Fluid Fine Tailings (FFT), and 2) temporal and spatial changes in porewater chemistry in Centrifuged Fine Tailings (CFT) during successive freeze-thaw-evaporation cycles. An anoxic laboratory batch experiment was conducted, where differing gypsum amendments were added to FFT, and destructively sampled over 64 weeks. Methane measured in the headspace showed inconclusive results for the effect of gypsum on methanogenesis. Gypsum-amended FFT showed an increase in dissolved salts, with Na increasing up to 1.3 times (820–1,100 mg L^{-1}) and Mg increasing up to 4.2 times (9.55–39.9 mg L^{-1}) compared to the control. In the second experiment, six columns filled with CFT were subjected to three consecutive freeze-thaw-evaporation cycles, and sacrificially sampled before each thaw and evaporative period. Column mass decreased an average total of 28.5 kg with 72% of this attributed to runoff following the first thaw period. After this time, dissolved salts began accumulating in near the CFT surface, with Cl increasing up to 5.8 times (379–2,200 mg L^{-1}), Na increasing up to 6.9 times (772–5,353 mg L^{-1}), K increasing up to 15.6 times (16.1–251 mg L^{-1}), and Mg increasing up to 94 times (22.0–2,069 mg L^{-1}) compared to the initial CFT. Both studies revealed elevated porewater salt concentrations in gypsum-amended tailings, which could pose challenges for long-term reclamation of the oil sands tailings.

ACKNOWLEDGEMENTS

I would first and foremost like to thank my advisor, Dr. Matt Lindsay. I am so grateful for the support and encouragement you have given me over the course of my degree. You have helped me grow as a scientist and writer, and your confidence in me and my abilities is greatly appreciated. Thank you to my committee member, Dr. Joyce McBeth, for your kindness and encouragement over the years. And thank you to my external examiner Dr. Kerry McPhedran for constructive feedback.

Thank you to the Syncrude Mine Closure Research Team for logistical support. Thank you to Adam Hammerlindl, Rafael Gonzalez, and Jim Rosen for assistance with data logger setup, to Adam Harrison at the Controlled Environment Facility for assistance setting up and monitoring the experimental chambers, and to Dr. Jing Chen for analytical support. A huge thank you to all the members of the Environmental Geochemistry Group, past and present. Noel, you are an amazing leader, and left some big shoes to fill. Sarah, thank you for being the best cheerleader, in and outside of work. Carlo, Lawrence, Aidan, Dan, Colton, James – you have all made such an impact on my life and career. Thank you all for being amazing friends.

Nicole, Christine, Sonja, thank you for keeping me sane during this degree, for always being there when I need a break from school and research. Wyatt and Shaina, thank you for the spontaneous visits and suppers, for going along this school journey together. Mum and Dad, thank you for everything. For your support and love and interest in my work, I would not be here without you guys. Atterberg and Kepler, I know you two cannot read, but you have been the best emotional support. Rém, thank you for being my rock, your unwavering love and support throughout this degree. I could not have done this without you.

TABLE OF CONTENTS

LIST OF TABLES

LIST OF FIGURES

LIST OF ABBREVIATIONS

AOSR	Alberta Oil Sand Region
CEC	Cation Exchange Capacity
CFT	Centrifuged Fine Tailings
EC	Electrical Conductivity
EDL	Electrical Double Layer
Eh	Reduction-Oxidation Potential
FFT	Fluid Fine Tailings
FTT	Froth Treatment Tailings
IC	Ion Chromatography
ICP-MS	Inductively Coupled Plasma–Mass Spectrometry
ICP-OES	Inductively Coupled Plasma–Optical Emission Spectroscopy
OSPW	Oil Sands Process Water
PES	Polyethersulfone
PVC	Polyvinyl Chloride
RH	Relative Humidity
rpm	rotations per minute
SRB	Sulfate Reducing Bacteria

CHAPTER 1: INTRODUCTION

The Alberta Oil Sand Region (AOSR) in northeastern Alberta, Canada, is over 140,000 km^2 in area, making it the third largest oil sands deposit in the world following Saudi Arabia and Venezuela (Allen, 2008; Small et al., 2015). The AOSR is divided into three deposits: the Athabasca deposit, the Cold Lake deposit, and the Peace River deposit. These deposits host proven reserves totalling 174 billion barrels of oil (approximately 27.7 trillion m^3; Allen, 2008; Small et al., 2015).

Three main geologic formations make up the AOSR: the Waterways Formation, the Wabiskaw-McMurray Formation, and the Clearwater Formation (Hein and Cotterill, 2006; Gibson et al., 2013). Most of the bituminous ore (~80%) occurs in the Cretaceous sand in the Wabiskaw-McMurray Formation, and is interbedded with shales, sands, and silts (Hein and Cotterill, 2006; Gibson et al., 2013; Small et al., 2015). The deeper Devonian Waterways Formation contains evaporate deposits within carbonate rock (Gibson et al., 2013). The Cretaceous Clearwater Formation is a shale unit that overlies the Wabiskaw-McMurray Formation, which is overlaid by Quaternary glacial till (Gibson et al., 2013).

The oil sand ore is loosely consolidated material, composed of approximately 12 wt. % bitumen, 84 wt. % mineral solids, and 4 wt. % water (Liu et al., 2005). Lower bitumen content does occur; however, it is not economical in Canadian standards to extract and upgrade the material, so the cut-off grade for processing is set at 7 wt. % bitumen (AER, 2016). A mixture of quartz sand, clay, and silt make up the solids, and water, bitumen, and trace gases fill the pore spaces (Lo et al., 2006). Bitumen is a heavy, unconventional oil with a viscosity greater than 1 kg m^{-1} s^{-1} and a density greater than 1,000 kg m^{-3} (Banerjee, 2012). Once bitumen is extracted

from the mineral solids, it is combined with diluent hydrocarbons to produce diluted bitumen or upgraded to synthetic crude oil and transported offsite for processing.

Two main approaches are used to extract bitumen from Alberta's oil sands deposits: *in situ* or by surface mining, with the latter being only feasible when the deposit is within approximately 80 m of original ground surface (Natural Resources Canada, 2016). Surface mining processes start with deforestation and removing the surface soil and overburden, which is stockpiled for later use in reclamation (Bergerson et al., 2012). When the oil sand deposit is exposed, the material is extracted and sent for further processing. There are two methods of *in situ* extraction that use steam injection to lower the viscosity of the bitumen and pumping it to the surface: cyclic steam simulation, and steam-assisted gravity drainage (Bergerson et al., 2012). Cyclic steam simulation uses one hole drilled vertically into the deposit, to inject steam and later remove bitumen (Alvarez and Han, 2013). Steam-assisted gravity drainage uses a pair of horizontal wells drilled under the deposit – one well is used to inject steam, and the second, lower well is used to remove the bitumen after it (Bolea et al., 2014). Although surface mining has higher recovery rates than *in situ*, surface mining can only be used for approximately 20% of the deposit area (4,800 km^2; Allen, 2008; Small et al., 2015). Because the Wabiskaw-McMurray formation dips to the southwest and sub-crops near the Athabasca River valley (north of Fort McMurray, Alberta), extraction in this region occurs via surface mining (Conly et al., 2002).

The extent of technical challenges and financial commitment for land reclamation is substantial. Extraction and upgrading of the oil sands produces large quantities of tailings that are temporarily stored in large tailings ponds to facilitate settlement and dewatering prior to permanent reclamation. The stricter timelines for mine closure plans (Government of Alberta, 2015),

generates the need for research focused on accelerating reclamation to minimize the tailings inventory.

1.1. BITUMEN EXTRACTION AND UPGRADING

Production of commercial petroleum products from mineable oil sands involves three key steps: (i) surface mining of bituminous ore, (ii) bitumen extraction from mined ore, and (iii) upgrading and offsite refining of extracted bitumen (Masliyah et al., 2004; Figure 1-1). In order to access the bituminous ore, the overlying trees and vegetation, muskeg, wetlands, topsoil, and overburden are removed to expose the bitumen-rich Lower Cretaceous strata (Gibson et al., 2013). The overburden is made up of sand, shale, silt, clay, and residual bitumen, which is at non-economic grades (Gray, 2015).

Oil sand ore is mined using truck and shovel methods that create large open pits that can reach several square kilometers in area (Masliyah et al., 2004; Liu et al., 2005). Ore is passed through crushers, breakers, and screens, then mixed with hot water, air, and process aids (e.g., sodium hydroxide, sodium citrate) to form a slurry (approximately 40% water, 6% bitumen, and more than 50% solids by weight; modified Clark Hot Water Extraction process; Clark, 1944; Daie and Chung, 1996; Gray, 2015). At specific concentrations, the addition of sodium hydroxide (NaOH) liberates the bitumen from the sand by producing surfactants from organic acids (Dai and Chung, 1996; Masliyah et al., 2004). Porewater from the McMurray Formation has naturally higher TDS (ranging up to 280 000 mg L^{-}), dominated by sodium and chloride (Gibson et al., 2013). Albertan oil sand has naturally higher concentrations of sodium (Na). The Na concentration is increased (up to an average of 880 mg L^{-1}; Dompierre et al., 2016) in oil sand process water (OSPW), as the water is recycled to limit net tailings volumes and to minimize water draw from natural surface water sources (e.g., the Athabasca River) (Masliyah et al., 2004;

Abolfazlzadehdoshanbehabazari et al., 2013; Foght et al., 2017; Figure 1-1). Large volumes of water are needed for the extraction of bitumen – in 2019, approximately 1.6 m^3 of water was used per barrel of oil equivalent (AER, 2019). Recycled water made up 78%, and nonsaline sources made up the rest (AER, 2019).

The slurry is transported via large-diameter hydrotransport pipelines to the extraction facility where material undergoes a water-based gravity separation process (primary separation) (Masliyah et al., 2004; Figure 1-1). The slurry is aerated by air bubbles, which attaches to bitumen in the pipelines (Gray, 2015). During primary separation, bitumen attaches to air bubbles which rise and form a froth (approximately 60% bitumen, 30% water, and 10% other solids) (Masliyah et al., 2004; Gray, 2015). At this stage, about 88−95% of bitumen is recovered (Masliyah et al., 2004). Coarser material sinks with gravity to the bottom of the vessel, producing primary separation tailings, also known as bulk tailings, which is hydrotransported to tailings facilities.

The recovered bitumen froth undergoes a hydrocarbon-based gravity separation process (froth treatment). The froth is de-aerated and diluent hydrocarbons are added to decrease viscosity (Masliyah et al., 2004; Gray, 2015). Two different diluents are used: a naphtha-based hydrocarbon or a paraffinic solvent (Masliyah et al., 2004; Gray, 2015). The decreased viscosity facilitates additional gravity separation of bitumen from water and fines, producing froth tailings which are hydrotransported to tailings facilities (Masliyah et al., 2004). Diluted bitumen may be upgraded on site to synthetic oil or sold directly to refineries off site (Syncrude, 2017).

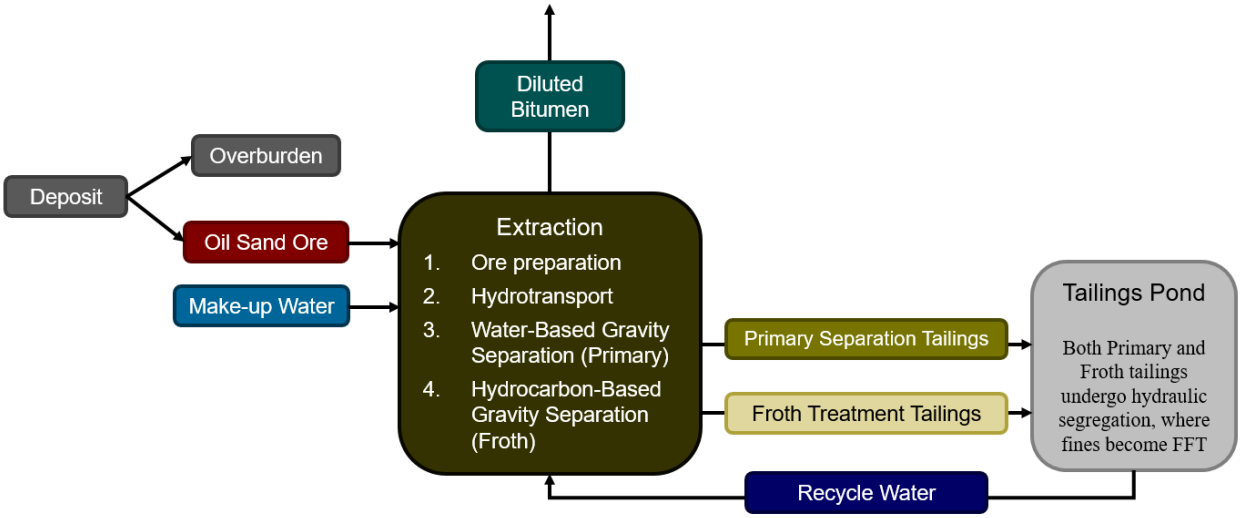

Figure 1-1: Simplified flow diagram of the oil sands mining and bitumen extraction process showing the two principal tailings streams produced during this process (modified from Mikula, 2012).

1.2. TAILINGS PRODUCTION

There are two main tailings streams at oil sands mines: (i) primary tailings, and (iii) froth treatment tailings (FTT) (Kasperski and Mikula, 2011). Primary tailings separate into coarse (sand) tailings and fluid fine tailings (FFT) during post-discharge segregation within tailings ponds. Coarse (sand) tailings are dominated by sand-sized particles that settle out immediately after discharge and form beach deposits (Kasperski and Mikula, 2011). FFT exhibits diluent hydrocarbons, and is dominated by clay- to silt-sized particles, which settle and dewater slowly in the tailings pond (Kasperski and Mikula, 2011; Dompierre et al., 2016). FTT is comprised of clay to sand-sized particles and generally exhibit low to moderate residual bitumen content (Kasperski and Mikula, 2011). These deposits exhibit potential for acid rock drainage and metal release due to an elevated sulfide-mineral content and potential for biogenic gas (e.g., methane, carbon dioxide) production due to the presence of residual diluent hydrocarbons (COSIA, 2012; Kasperski and Mikula, 2011; Lindsay et al., 2019).

1.2.1 Tailings Ponds and Fluid Fine Tailings

Tailings ponds, also referred to as settling basins, are temporary storage facilities for tailings until permanent reclamation occurs. These ponds currently cover an area of over 180 km^2 in the AOSR, and as of 2019, hold about 1,303 x 10^6 m^3 of fluid tailings (AER, 2020). Fluid tailings is any fluid from extraction with more than 5 wt. % suspended solids and an undrained shear strength of less than 5 kPa (AER, 2017). Tailings ponds often include four distinct zones: beach deposits near discharge points, the water cap layer, the tailings-water interface, and fine tailings solids that become thicker and coarser with depth (Small et al., 2015). These zones develop over time, through settlement and dewatering based on tailings material composition. Tailings ponds may be used for temporary storage of various tailings streams including FFT, coarse sand tailings and FTT, plus bitumen upgrading byproducts like petroleum coke.

Fluid fine tailings are primarily made up of clay-sized particles, with a particle size of less than 44 μm, and a mean of 5−10 μm (Kasperski and Mikula, 2011). The solids content in FFT is anywhere between 20−80 wt. % clays and silts, becoming denser with depth (Small et al., 2015); however, FFT is commonly reported at approximately 20−30 wt. % solids, 70−80 wt. % water, and 1−3 wt. % residual bitumen (Allen, 2008). High concentrations of total dissolved solids (TDS; 2000−2500 mg L^-) are present in the porewater (OSPW), dominated by sodium (Na; 500−840 mg L^-), bicarbonate (HCO_3), chloride (Cl; 75−700 mg L^-), and sulfate (SO_4; 0−530 mg L^-) (Allen, 2008; Heaton, 2015).

Fluid fine tailings have an initial minimum solids content of 2 wt. % (COSIA, 2012). It can take 3−5 years to reach 30 wt. % solids in FFT through natural consolidation (BGC Engineering, 2010; Siddique et al., 2014; Heaton, 2015). Futher dewatering can take decades or more, due to the negative repulsive charge of clay particles which prevent aggregation (BGC

Engineering, 2010; Heaton, 2015). Clay mineralogy dictates how the FFT will settle in the water column. Once FFT exceeds 30 wt. % solids, and has settled for several years, it is sometimes referred to as mature fine tailings (Allen, 2008; COSIA, 2012).

1.2.2 Clay Mineralogy

The predominant clay minerals found in FFT are kaolinite [$Al_2Si_2O_5(OH)_4$], illite [$K_{0.65}Al_{2.0}[Al_{0.65}Si_{3.35}O_{10}](OH)_2$], and chlorite ($A_{5\text{-}6}T_4Z_{18}$, where A = Al, Fe^{2+}, Fe^{3+}, Li, Mg, Mn, or Ni; T = Al, Fe^{3+}, Si, or a combination; Z = O and/or OH), with the first two composing the majority of clay in FFT (Hooshiar et al., 2012; Heaton, 2015; Dompierre et al., 2016; Cilia, 2017).

Clay minerals are composed of different layering patterns of tetrahedral (SiO_4) and octahedral sheets (Barber, 1984; Barton and Karathanasis, 2002). Octahedrons are made up of a central cation (divalent or trivalent), surrounded by six oxygen or hydroxyl groups (Sposito et al., 1999; Barton and Karathanasis, 2002). When the central cation is divalent (e.g., Mg^{2+}, Fe^{2+}), the cation-site occupancy (3 total) is full, and is referred to as trioctahedral (Sposito et al., 1999; Barton and Karathanasis, 2002; Bleam, 2017). When the central cation is trivalent (e.g., Al^{3+}, Fe^{3+}), one third of the cation sites are left empty, and this is referred to as dioctahedral (Sposito et al., 1999; Barton and Karathanasis, 2002; Bleam, 2017). Distinct clay minerals are created by differing sheet arrangements and substitutions. Clays with 1:1 layer type have one tetrahedral sheet and one octahedral sheet (e.g., kaolinite); clays with 2:1 layer type have one octahedral sheet between two tetrahedral sheets (e.g., illite); and clays with 2:1:1 layer type have the same structure as 2:1 clays, with an interlayer brucite or gibbsite sheet (e.g., chlorite; Barber, 1984; Sposito et al., 1999; Barton and Karathanasis, 2002).

Cations with comparable ionic radii can replace each other in an octahedral and tetrahedral sheets in clay minerals (Barber, 1984; Barton and Karathanasis, 2002). This permanent

replacement is called isomorphic substitution, and can create either positive or negative charge imbalances; however, a net negative charge is more common (Barton and Karathanasis, 2002). This charge is structural and is continuous regardless of any changes in the surrounding solution's pH and chemistry (Sollins et al., 1988).

Variable charges can occur at the edge of broken clay minerals in octahedral layers, which are exposed to bulk solution in 1:1 clays and at the edges of 2:1 clays (Barber, 1984; Shainberg and Levy, 2005). These charges are based on the pH of the surrounding solution, where a negative charge occurs with a higher pH and a positive charge occurs with a lower pH, with the point of zero net proton charge typically being at a pH of 3-4 (Barber, 1984; Sollins et al., 1988; Langmuir, 1997; Shainberg and Levy, 2005). Because OSPW has an average pH of 8.0-8.4, these sites in FFT clays are negatively charged (Heaton, 2015). Although clays have both structural and variable charges, structural charges are dominant in systems with neutral to alkaline pH and relatively stable conditions (Sollins et al., 1988). In OSPW, only structural charges play a significant role.

1.2.3 Cation Exchange Capacity and Electrical Double Layer

Cation exchange capacity (CEC) refers to the net number of charges on negatively charged clay minerals that attract hydrated cations to achieve a neutral charge (Osacky et al., 2014). It is important to note that a single charge on a clay mineral is not necessarily occupied by one cation. Monovalent cations (e.g., Na^+) can only occupy one charge per cation; meanwhile, one multivalent cation can occupy the same number of charges on a clay mineral as the charge of the cation. CEC can vary with structure of the clay mineral, interlayering scenarios, surface area, and particle size (Osacky et al., 2014).

The electrical double layer (EDL) describes the distribution of cations and anions on or in close proximity of a mineral's surface in a solution (Konhauser, 2007). There are multiple models describing the distribution of ions within the EDL. One of these theories splits the ions into two layers: the Stern layer and the Gouy layer (Figure 1-2) (Konhauser, 2007). The Stern layer encompasses ions fixed on the mineral surface, and is dominated by hydrated ions exhibiting opposite charge to the net structural charge of the mineral surface (Konhauser, 2007). The next outer layer away from the mineral's surface is the Gouy layer, which has both anions and cations that are attracted to the surface via electrostatic forces (Konhauser, 2007). Oppositely charged ions still dominate in the Gouy layer, though they are blocked from the surface of the clay mineral by the hydrated ions in the Stern layer (Konhauser, 2007). The bulk solution refers to any other ions in the surrounding solution, where there is an approximate even charge distribution between anions and cations.

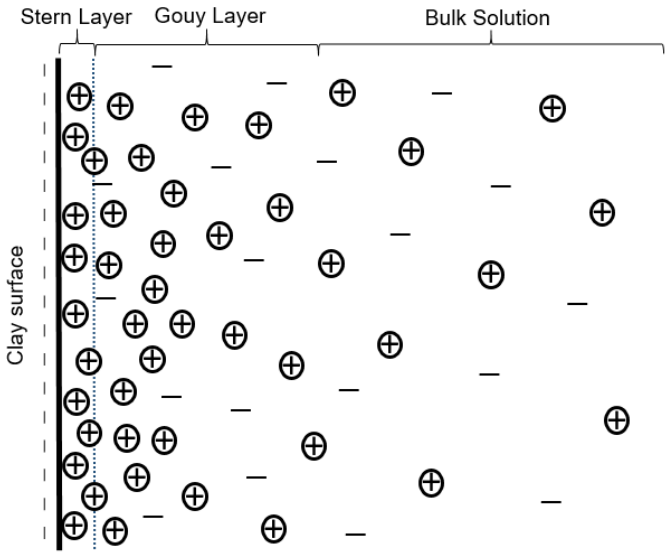

Figure 1-2: The Stern layer and Gouy layer describes the distribution of anions and cations on or close to a negatively charged clay mineral. The surrounding bulk solution continues away from the mineral (after Konhauser, 2007).

The EDL thickness decreases when an excess of multivalent ions compared to monovalent ions are present in solution, requiring less multivalent ions to acquire a net neutral charge (Ugochukwu, 2019). When the bulk solution is dominated by Na, the EDL can be as large as 50 nm, while divalent cation saturated solutions can have EDL thicknesses of 0.5-1.0 nm (Barber, 1984). Monovalent cations will be more dispersive to individual clay minerals, reducing clay coagulation and inhibiting settlement and dewatering of the clay matrix. As long as a net neutral charge is achieved, divalent cations allow for a closer packing of clay minerals.

1.3. TAILINGS RECLAMATION

The Alberta Energy Regulator (AER) created Directive 074 in 2009, to help curb the growing FFT inventories, and set standards for all projects to help slow the rate of FFT production (AER, 2017). Due to inconsistencies in methods to measure FFT volumes and reporting between sites, the AER then used the Tailings Management Framework for the Mineable Athabasca Oil Sands to implement Directive 085, which replaced Directive 074 (2017). Improved standards in Directive 085 created consistency and considered both current and future fluid tailings inventories, with specific requirements for inspections and evaluations, planning requirements, and reporting (Government of Alberta, 2015; AER, 2017). These requirements are enforced, and failure to follow them may result in shut down of operations, financial penalties, and/or prosecution (Government of Alberta, 2015). Together, Directive 085 and the Tailings Management Framework ensures that all tailings will be treated and reclaimed during mine operations and will be in a ready-to-reclaim state 10 years after the mine has closed (Government of Alberta, 2015; AER, 2017). In order to meet this requirement, operators are developing various technologies to manage FFT throughout the lifetime of mines (new and existing), and creating transparency with continuous reporting (Government of Alberta, 2015; AER, 2017).

Tailings treatment technologies include (alone or in combinations): the addition of flocculants (e.g., polyacrylamide) and/or coagulants (e.g., alum, gypsum), centrifugation, co-mixing (e.g., composite tailings), water-capped tailings, and thin lift dewatering (Masliyah et al., 2004; BGC Engineering, 2010; Kasperski and Mikula, 2011; COSIA, 2012). These technologies support progressive reclamation in aquatic and terrestrial landforms, thereby minimizing growth of fluid tailings inventories as outlined in Directive 085 (Kasperski and Mikula, 2011; COSIA, 2012; Foght et al., 2017).

Aquatic reclamation involves the creation of water bodies (i.e., end pit lakes), including wetlands (COSIA, 2012; Foght et al., 2017). End pit lakes are permanent reclamation landforms created from inactive open mine pits, with a long-term goal to become self-sustaining and integrating with the regions hydrologic system (COSIA, 2012; Dompierre et al., 2017; Foght et al., 2017; Kabwe et al., 2019). Up to 32 end pit lakes have been proposed in mine closure plans in the AOSR, with 8 of them containing both water-capped FFT and treated FFT (Kabwe et al., 2019).

Terrestrial reclamation involves the removal of water to create stability and strength in the tailings material to achieve trafficable surfaces on landforms (BGC Engineering, 2010; COSIA, 2012; Foght et al., 2017). The tailings are dewatered through mechanical processes and freeze-thaw cycles in disposal cells, where further dewatering occurs (BGC Engineering, 2010; COSIA, 2012). After sufficient water is removed, the material can be used as a landscape builder and capped with a sand and soil mixture to limit erosion and support plant growth (COSIA, 2012).

1.3.1 Gypsum

Gypsum [$CaSO_4 \cdot 2H_2O$] addition to fluid tailings is currently being explored as an aid to increase dewatering. Gypsum, a hydrated calcium sulfate, will dissociate into calcium (Ca^{2+}) and sulfate (SO_4^{2-}) when added to water (Equation 1.1; Small et al., 2015). Calcium is a divalent cation

and can replace two monovalent sodium (Na^+) ions (Equation 1.2), decreasing the EDL thickness and allowing for a closer packing of clay minerals (Figure 1-3; Holden et al., 2011). The hydrated radius of Ca and Na are pretty similar (0.41 nm and 0.36 nm, respectively), even though the Ca has double the charge (Israelachvili, 2011). With the replacement of Na^+, the water in the hydrated radius of individual Na^+ cations is also removed.

$$CaSO_4 \cdot 2H_2O \rightleftharpoons Ca^{2+} + SO_4^{2-} + 2H_2O \qquad \text{Equation 1.1}$$

$$Ca^{2+} + 2Na\text{-}X \rightleftharpoons Ca\text{-}X + 2Na^+ \qquad \text{Equation 1.2}$$

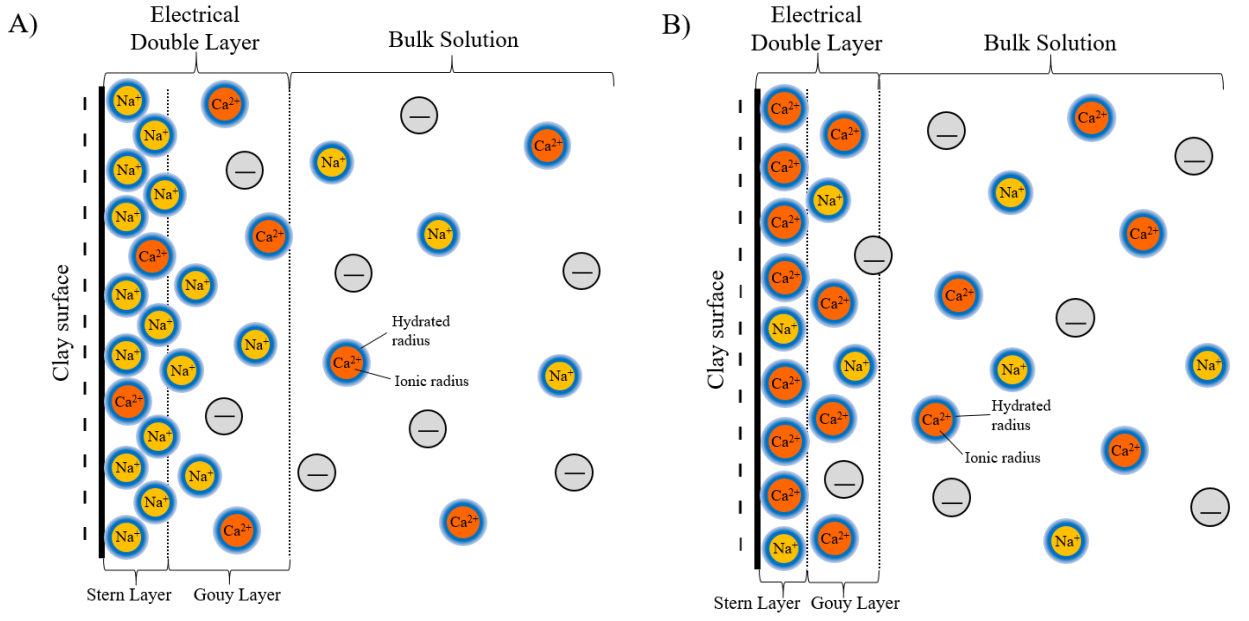

Figure 1-3: The Electrical Double Layer for a negatively charged clay mineral is larger in A) where Na^+ is the dominant cation compared to B) where Ca^{2+} is also abundant.

1.3.1.1 Biogeochemical Implications

Past studies have shown the presence of methanogens in oil sand tailings, which can enhance consolidation in tailings (Fedorak et al., 2003; Siddique et al., 2012; Foght et al., 2017). Increasing methane concentrations can lead to exsolution (bubble formation) and ebullition (bubble transport)), which can create channels through the fine material and allow the release of porewater (BGC Engineering, 2010; Siddique et al., 2014). Methanogens also produce carbon dioxide (CO_2), which decreases pH (Siddique et al., 2014). With this decrease, dissolution of carbonate minerals

occurs and divalent cations are released (i.e., Ca^{2+}, Mg^{2+}), which can exchange for Na^{+} on clay minerals and promote exchange and dewatering (Siddique et al., 2014).

Methanogenesis within oil sand tailings ponds can also have negative implications (Foght et al., 2017). Degradation of residual diluent hydrocarbons (including *n*-alkanes, *iso*-alkanes, and monoaromatics) are broken down by methanogens (Siddique et al., 2012; Foght et al., 2017; Kong et al., 2019). This biodegradation produces two greenhouse gases: carbon dioxide (CO_2) and methane (CH_4) (Brown et al., 2013; Stasik and Wednt-Potthoff, 2016; Foght et al., 2017; Kong et al., 2019). Methane ebullition can occur when dissolved CH_4 concentrations reach solubility limits and form bubbles (i.e., exsolution). If these bubbles grow sufficiently large and buoyant enough to overcome the FFT shear strength, they may be transported upward through the FFT, across the FFT-water interface, and through the water cover before being released to the atmosphere (Holowenko et al., 2000; Foght et al., 2017; Kong et al., 2019). Methane can also be trapped in the tailings, creating voids and increasing the volume of tailings (Holowenko et al., 2000; Foght et al., 2017). In the water, dissolved CH_4 and O_2 can be consumed by methanotrophs, leading to decreased oxygen concentrations in the environment, thereby inhibiting the growth and survival of plants and animals (Holowenko et al., 2000; Foght et al., 2017). Carbon dioxide generated during methanogenesis and methanotrophy can increase dissolved CO_2 and decrease pH, as described above (Siddique et al., 2014).

The presence of sulfur reducing bacteria (SRB) in tailings ponds has been confirmed, through previous research in microbial analysis and analysis of sulfate and sulfide in tailings (Foght et al., 2017). SRB play key roles in sulfur and carbon cycling within these systems (Stasik and Wednt-Potthoff, 2016; Foght et al., 2017). The addition of gypsum to tailings increases dissolved sulfate concentrations, which acts as an electron acceptor for SRB (Foght et al., 2017).

SRB catalyzes sulfate reduction, and coupled with organic carbon (CH_2O) oxidation, produces bicarbonate (HCO_3^-), bisulfide (HS^-), and protons (H^+) (Equation 1.3; Bethke et al., 2008). If porewater pH is less than 7, the bisulfide and protons can further react to form hydrogen sulfide (H_2S) (Equation 1.4) (Ong, 2007; Bethke et al., 2008). However, FFT porewater is rarely below pH 7, and the potential emission of H_2S would only occur in the presence of high pCO_2 from microbial respiration processes (Ong, 2007; Bethke et al., 2008; Foght et al., 2017). Any H_2S emissions could be minimized in the presence of iron, with the formation of iron sulfide precipitates (Heaton, 2015; Foght et al., 2017).

$$SO_4^{2-} + 2CH_2O \rightleftharpoons 2HCO_3^- + HS^- + H^+ \quad \text{Equation 1.3}$$

$$HS^- + H^+ \rightleftharpoons H_2S\,(aq) \quad \text{Equation 1.4}$$

Methanogens and SRB can utilize the same electron donors (hydrogen, acetate), creating competition between microbes (Bethke et al., 2008; Ramos-Padrón et al., 2011; Stasik and Wednt-Potthoff, 2016). Methanogenesis may be suppressed when SO_4, derived from gypsum or other sources, is added and the useable energy available to SRB exceeds that of methanogens (Bethke et al., 2008; Ramos-Padrón et al., 2011; Brown et al., 2013; Stasik and Wednt-Potthoff, 2016). However, if there is an abundance of electron donors in the system through hydrocarbon degradation, methanogens and SRB can co-exist, perhaps in close proximity (Holowenko et al., 2000; Stasik and Wednt-Potthoff, 2016). Understanding the dynamics of H_2S, CH_4, and CO_2 production following gypsum addition is critical for assessing potential implications of this tailings technology for aquatic and terrestrial reclamation landscapes.

1.3.2 Treated Tailings

Syncrude Canada Ltd. use a method to treat tailings through decanter centrifugation. After a few years of consolidation within tailings ponds (achieving a maximum of 30 wt. % solids), FFT

is dredged, combined with gypsum and anionic polyacrylamide to aid in coagulation and flocculation, and decanter-centrifuged to promote dewatering (BGC Engineering, 2010; COSIA, 2012; Heaton, 2015). A portion of divalent Ca^{2+} from gypsum exchanges for monovalent Na^{+} on clay minerals, decreases EDL thickness and allows for closer packing of clay minerals (Heaton, 2015). Polyacrylamide creates bridges between clay minerals, forming larger and heavier particles that will naturally settle faster in the water column (BGC Engineering, 2010). The mixture is subjected to acceleration many times that of gravity, creating centrifuged fine tailings (CFT) (Rima and Azam, 2015). The resultant material has a water content of 50 – 58 wt. % and is deposited in thin layers (< 2 m) by truck end dumping (Heaton, 2015). For ongoing dewatering, each layer is subjected to one seasonal freeze-thaw cycle, reducing the water content in the CFT to less than 30 wt. %, before another layer is deposited (Heaton, 2015). It is currently unknown how the freeze-thaw process affects chemistry and distribution of released porewater in CFT. The movement of salt through CFT and potential for evaporative salt at the surface may lead to problems in future solid landscape reclamation efforts (Fedorak et al., 2003). Even with a reclamation soil cover, salts can still persist and create challenges for revegetation and water quality (Vessey et al., 2019).

CHAPTER 2: RESEARCH SCOPE

Various technologies are being developed and implemented to accelerate dewatering of fluid tailings. Research is continuing to understand the biogeochemical implications of adopting these technologies. Field studies which focus on CFT treated with gypsum and polyacrylamide suggest an increase in both microbial sulfate reduction and dissolved salt concentrations, which strongly affect water chemistry and, therefore, reclamation capability. This thesis integrates two laboratory experiments to further explore these issues: (i) batch experiment to assess temporal changes in porewater chemistry and gas production in gypsum-amended FFT; and (ii) column experiment to examine temporal and spatial changes in porewater chemistry in CFT during successive freeze-thaw-evaporation cycles. These experiments will test two key ***research hypotheses***:

- gypsum addition stimulates sulfate reduction and inhibits methanogenesis; and
- freeze-thaw-evaporation cycles concentrate salts near the tailings surface.

Specific ***research objectives*** related to the batch and/or column experiments are to:

- examine temporal and spatial changes in porewater chemistry;
- assess temporal changes in carbon dioxide and methane production;
- determine temporal changes in salt distribution; and
- identify potential implications for mine closure.

CHAPTER 3: BATCH EXPERIMENTS

The implications of gypsum addition for water chemistry and gas (i.e., CO_2, CH_4, H_2S) production within FFT deposits are not fully understood. Therefore, laboratory batch experiments were conducted to examine the temporal changes in gas production and porewater chemistry associated with different gypsum amendment rates. These findings will help inform ongoing development of tailings technologies, while minimizing secondary effects from a gypsum amendment.

3.1. FLUID FINE TAILINGS

FFT used in the batch experiments were collected from Base Mine Lake, located at the Syncrude Canada Ltd. Mildred Lake Mine (also known as Base Mine) about 35 km north of Fort McMurray, Alberta, Canada. Base Mine Lake was the first oil sands end pit lake and commercial-scale demonstration of water capped tailings technology in the AOSR. This end pit lake was officially commissioned in December 2012, after approximately 186M m^3 of FFT had been pumped into the former West-In-Pit over the preceding 18 years. Base Mine Lake covers a 7.8 km^2 area and, as of October 2012, contained up to 48 m of FFT submerged under a water cap that averaged 6.5 m deep. The water cap depth increased to between 8 and 12 m by 2018 due to *in situ* FFT settlement and dewatering (Dompierre et al., 2017). These tailings increase in solids content with depth, ranging from approximately 20 % (w/w) near the tailings-water interface to over 50 % (w/w) deeper in the FFT profile (Dompierre et al., 2016). FFT porewater has high concentrations of Ca, Na, Mg, K, and Cl, and low Fe concentrations (Dompierre et al., 2016). Porewater pH is circumneutral (i.e., 6.6 to 8.3) and anoxic conditions extend from immediately

below the tailings-water interface through the FFT profile (Dompierre et al., 2016; Rudderham, 2019; Francis, 2020).

FFT was collected for this experiment in October, 2016, at sampling Platform 1, located near the center of Base Mine Lake. The material was taken at 14.6 m below the water surface (approximately 5.5 m below the tailings-water interface), using a purpose-built sampling boat with a pneumatic fluid sampler (see Dompierre et al., 2016 for details). Subsequent sampling was conducted in 2016 and 2017 at or near Platform 1 by Rudderham (2019) and Francis (2020). At Platform 1, FFT porewater EC was approximately 3.9 mS cm^{-1} at 5.5 m, and had an overall increase with depth, correlating to an increase in Na^+, Cl^-, and HCO_3 concentrations (Dompierre et al., 2016; Rudderham, 2019). Methane production (average = 45 mg L^{-1} at Platform 1, between 2.5 and 7.5 m below the tailings-water interface) and evidence of anaerobic microbial communities (e.g. methanogens and SRB) have been found at this location, proving it is naturally an anaerobic environment (Rudderham, 2019; Francis, 2020).

3.2. EXPERIMENTAL SETUP

The FFT was homogenized using a paint mixer and 100 g $\pm$ 0.05 g of FFT was added to 120 mL amber glass serum bottles (Wheaton) in a fume hood. The gravimetric moisture content of the FFT was on average 20.5%, resulting in an equivalent dry weight of 79.5 g dry FFT added per bottle. The bottles were immediately transferred into an anoxic chamber and allowed to equilibrate with the atmosphere ($\leq$ 5 vol% $H_{2(g)}$, balance $N_{2(g)}$) for 24 h. The anoxic atmosphere represented the environment the FFT was sampled from, and allow for anaerobic microbial activity.

Gypsum [$CaSO_4 \cdot 2H_2O$] (98 % purity, Sigma-Aldrich) was then added to the bottles to achieve a range of amendment rates based on preliminary experiments (mg g^{-1} dry FFT):

0.00 (control), 0.25, 0.50, 1.00, 2.00 (Table 2-1). These rates are based on a target rate of 1.5 kg t^{-1} dry FTT reported by Heaton (2015) for the Syncrude centrifugation process. Triplicates were prepared to assess the reproducibility of experimental results, for a total of 105 individual batches (Table 2-1). The bottles were capped with grey bromobutyl rubber stoppers (VWR, 89236-132), crimp sealed with aluminum caps (VWR, 16171-896), and thoroughly mixed by swirling the bottle. Triplicate samples were destructively sampled seven times over 64 weeks (Table 2-1).

Table 2-1: Gypsum amendment rate and sampling schedule for batch experiment, using triplicate samples. Sampling was performed on three consecutive days, where (a) was sampled on Monday, (b) was sampled on Tuesday, and (c) was sampled on Wednesday.

Sample ID	Gypsum (mg g^{-1} dry FFT)	Elapsed Time (weeks)						
		0	2	4	8	16	32	64
MC-0.00	0.00	a, b, c	a, b, c	a, b, c	a, b, c	a, b, c	a, b, c	a, b, c
MC-0.25	0.25	a, b, c	a, b, c	a, b, c	a, b, c	a, b, c	a, b, c	a, b, c
MC-0.50	0.50	a, b, c	a, b, c	a, b, c	a, b, c	a, b, c	a, b, c	a, b, c
MC-1.00	1.00	a, b, c	a, b, c	a, b, c	a, b, c	a, b, c	a, b, c	a, b, c
MC-2.00	2.00	a, b, c	a, b, c	a, b, c	a, b, c	a, b, c	a, b, c	a, b, c

3.3. GAS SAMPLING AND ANALYSIS

Headspace gases within the serum bottles were collected and analyzed at pre-determined time intervals based on preliminary experiments (Table 2-1). Gas-tight glass syringes (5 mL; Vici, A-2 series, Vici, USA) were flushed three times with ultrapure $He_{(g)}$ (99.999 %, Praxair, Canada) and then filled with $He_{(g)}$ (5.5 cc, 1 atm) and transferred into the anaerobic chamber. The $He_{(g)}$ was injected into the headspace (46.2 cc) and allowed to mix before the same volume of sample (5.5 cc) was drawn back into the syringe. The syringe was removed from the anaerobic chamber for quantification of $CH_{4(g)}$ and $CO_{2(g)}$ by gas chromatography (Model 490, Agilent Technologies, USA).

The gas chromatograph used helium gas as a carrier gas, because of its high thermal conductivity, and a 10 m PortPLOT U column (Agilent Technologies, USA). The column and injection temperature were set at 50.0 ^{o}C, the column pressure was set at 150.0 kPa, and the injection time was 40 ms. Calibration curves were generated by analyzing certified gas standards (Praxair, USA) and ambient air samples before each group of 10 samples. Based on availability, the gas standards included combinations of: (1) 10% CO_2, 10% CH_4, He balanced (Praxair, 990787, USA), (2) 5,000 ppm CO_2, N_2 balanced (Praxair, 973272, USA), (3) 100 ppm CH_4, N_2 balanced (Praxair, 979937, USA), and (4) 20% CO_2, 20% CH_4, N_2 (Praxair, 990725, USA). Dissolved gases were calculated using Henry's constants, based on values reported by Benson and Krause (1976) and Wilhelm et al. (1977) (Jones et al., 2014).

3.4. POREWATER SAMPLING AND ANALYSIS

Following headspace gas sampling, the serum bottles were vigorously mixed by hand for 10 s to mix FFT and released water. The bottles were then opened and FFT was transferred into two separate sterile 50 mL polypropylene conical centrifuge tubes (VWR, USA). These tubes were capped, removed from the anaerobic chamber, and centrifuged at 13,800 x g (10,000 rpm) for 20 min (Eppendorf, model 5804 R, Germany).

The following tests were completed on the bench, outside of the anaerobic chamber. Reduction-oxidation (redox) potential (Eh), pH, hydrogen sulfide (ΣH_2S), and alkalinity were measured immediately after centrifugation. Prior to performing these measurements, the supernatant was passed through 0.45 µm polyesthersulfone (PES) syringe filter membranes (Pall Corporation, USA) using sterile syringes (HSW GmbH, Germany). The pH electrode (Thermo Orion, model 8156BNUWP, USA) was calibrated to NIST traceable pH 4, 7, and 10 buffer solutions, and the calibration was rechecked between each measurement. The Eh electrode

(Thermo Orion, model 9678BNWP, USA) performance was confirmed using Zobell's (Nordstrom, 1977) and Light's (Light, 1972) solutions. Dissolved H_2S concentrations were determined by spectrophotometry (Hach, model DR 2800, USA) using a modified Hach Method 8131 (Hach Chemical Co., 2018). This method was adapted for 1 mL cuvettes, using a single wavelength with an absorbance of 665 nm. Absorbance was compared to standard curves created using a methylene blue calibration standard for H_2S (RAD 171, Sigma Aldrich, USA). Alkalinity was determined by titration (Hach, Method 8203, USA) with normalized sulfuric acid (H_2SO_4; 1.600 ± 0.008 N) to the bromocresol green methyl red (Ricca Chemical Company, USA) end point.

Additional supernatant samples were collected and preserved for quantification of inorganic anions, major elements, and trace elements. Inorganic anion samples were first passed through 0.45 µm PES syringe filter membranes and analyzed by ion chromatography (IC; EPA Method 300.0). Major element and trace element samples were passed through 0.1 µm PES syringe filter membranes, acidified to pH <2 with trace element grade nitric acid (HNO_3; Omnitrace, EMD Millipore, USA), and analyzed by inductively coupled plasma–optical emission spectroscopy (ICP–OES; EPA Method 200.7) and inductively coupled plasma–mass spectrometry (ICP–MS; EPA Method 200.8), respectively. All water samples were stored in clean high-density polyethylene bottles and refrigerated (4°C) between collection and analysis.

3.5. RESULTS

3.5.1 Dissolved Methane and Carbon Dioxide

Dissolved CO_2 concentrations ranged from 4.82 mg L^{-1} (MC-0.25, week 0) to 129 mg L^{-1} (MC-2.00, week 64) over the course of the experiment (Figure 3-1). CO_2 concentrations increased sharply from <10 mg L^{-1} at week 0 to between 51.8 mg L^{-1} (MC-0.25) and 105.7 mg L^{-1}

(MC-2.00) at week 2. Concentrations were relatively stable from week 8 to week 64 sampling times, ranging from 48.6 mg L^{-1} (MC-0.00) to 129.3 mg L^{-1} (MC-2.00). In general, both the gypsum amendment rate and dissolved CO_2 concentrations increased over the same time period, with observed increases principally observed between 0 and 2 weeks.

Dissolved CH_4 concentrations ranged from 0.62 g L^{-1} (MC-0.25, week 0) to 25.1 mg L^{-1} (MC-0.50, week 8) over the course of the experiment (Figure 3-1). CH_4 concentrations increased sharply from <2 mg L^{-1} at week 0 to between 5.8 mg L^{-1} (MC-0.00) and 13.5 mg L^{-1} (MC-0.50) at week 2. Concentrations continued to increase to between 15.9 mg L^{-1} (MC-0.00) and 25.0 mg L^{-1} (MC-0.50) at week 8. During week 32, a slight decrease occurred in CH_4 concentrations for MC-2.00, with concentrations being lower than the other amendments. The remainder of the experiment showed a positive trend between gypsum amendment rate and CO_4 concentrations.

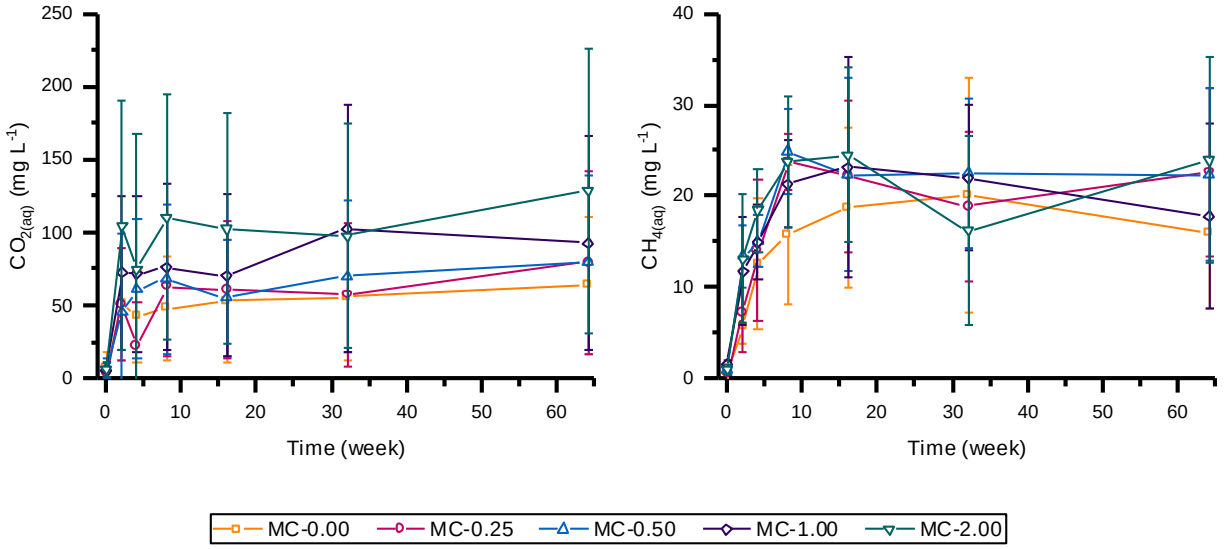

Figure 3-1: Dissolved carbon dioxide and methane concentrations in the water. Error bars are one standard deviation.

3.5.2 Porewater Chemistry

3.5.2.1 pH, Eh, and Alkalinity

Porewater pH ranged from 7.56 (MC-2.00, week 64) to 8.12 (MC-0.00, week 0) during the experiment (Figure 3-2). At week 0, pH ranged between 7.86 (MC-2.00) to 8.12 (MC-0.00), and gradually decreased to week 64, where pH was between 7.56 (MC-2.00) and 7.92 (MC-0.00). A slight increase at week 32 was observed in all gypsum treatments and the control. Overall, with increasing concentrations of gypsum there is a decrease in pH. This is consistent with the increase of CO_2 concentrations, as dissolved CO_2 will increase the hydrogen ions in water and decrease pH.

Redox potential (Eh) in porewater ranged from 210 mV (MC-0.50, week 64) to 430 mV (MC-0.00, week 8) over the course of the experiment (Figure 3-2). Eh values were relatively stable between week 0 and week 4, ranging between 268 mV (MC-1.00, week 2) and 327 mV (MC-0.00, week 2). Week 8 saw Eh values increase, ranging from 350 mV (MC-1.00) to 430 mV (MC-0.00), then gradually decrease to week 64. Throughout the experiment the Eh values remained positive and there was no obvious trend between differing gypsum amendments.

Alkalinity in porewater (reported as $CaCO_3$) ranged from 699 mg L^{-1} (MC-1.00, week 4) to 1,250 mg L^{-1} (MC-0.00, week 64) over the course of the experiment (Figure 3-2). These concentrations are consistent with reported values of alkalinity in FFT, ranging from 650 mg L^{-1} to 1,400 mg L^{-1} (Allen, 2008; Fedorak et al., 2003; Holowenko et al., 2000; Siddique et al., 2014). Week 0 had alkalinity concentrations that ranged from 947 mg L^{-1} (MC-1.00) to 1,100 mg L^{-1} (MC-0.25), then decreased to week 4 where alkalinity was between 700 mg L^{-1} (MC-1.00) and 1,014 mg L^{-1} (MC-0.00). Alkalinity concentrations then increased to week 64, ranging from 893 mg L^{-1} (MC-2.00) and 1,253 mg L^{-1} (MC-0.00). An overall inverse trend between gypsum addition and alkalinity concentrations was observed.

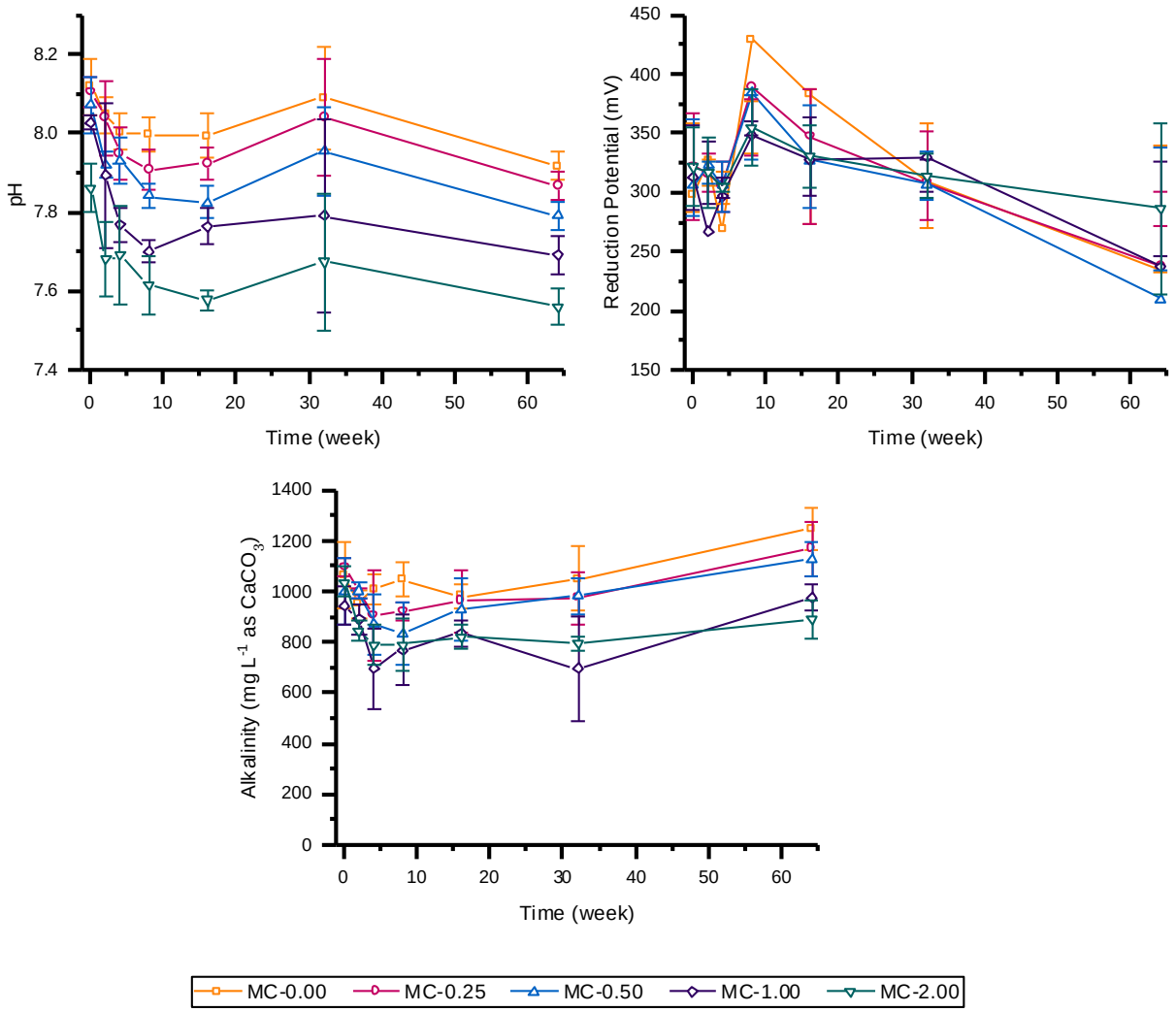

Figure 3-2: Porewater pH, reduction-oxidation potential (Eh), and alkalinity (mg L^{-1} as $CaCO_3$) for the batch experiment. Error bars are one standard deviation.

3.5.2.2 Major Cations

Porewater Ca concentrations ranged from 17.0 mg L^{-1} (MC-0.00, week 64) to 149 mg L^{-1} (MC-2.00, week 16) over the course of the experiment (Figure 3-3). In both MC-1.00 and MC-2.00, Ca concentrations exhibited an initial increase from week 0 (43.4 mg L^{-1} and 111 mg L^{-1}, respectively) to week 2 (61.7 mg L^{-1} and 147 mg L^{-1}, respectively), then remained relatively consistent to week 64. This plateau possibly indicates the maximum exchange capacity

on the clays had been reached. The concentrations from week 0 onwards in MC-0.00, MC-0.25, and MC-0.50 were stable throughout the experiment, ranging from 17.0 mg L^{-1} (MC-0.00) and 35.7 mg L^{-1} (MC-0.50). An overall positive trend between Ca concentrations and increasing gypsum amendment rates was observed.

Sodium concentrations in porewater ranged from 820 mg L^{-1} (MC-0.00, week 8) to 1,100 mg L^{-1} (MC-2.00, week 32) over the course of the experiment (Figure 3-3). At week 0 Na concentrations ranged between 824 mg L^{-1} (MC-0.00) to 1,050 mg L^{-1} (MC-2.00), and gradually increased to week 32, where concentrations were between 864 mg L^{-1} (MC-0.00) and 1,136 mg L^{-1} (MC-2.00). Na concentrations decreased slightly between week 32 and week 64, ending between 862 mg L^{-1} (MC-0.00) and 1,111 mg L^{-1} (MC-2.00). An overall positive trend occurred between Na concentrations and increasing gypsum amendment rates.

Magnesium concentrations had a range of 9.55 mg L^{-1} (MC-0.00, week 64) to 39.9 mg L^{-1} (MC-2.00, week 16) over the course of the experiment (Figure 3-3). Mg concentrations exhibited an initial increase in both MC-1.00 and MC-2.00 between week 0 (16.9 mg L^{-1} and 31.4 mg L^{-1}, respectively) and week 2 (22.6 mg L^{-1} and 38.2 mg L^{-1}, respectively), then remained relatively consistent to week 64. Mg concentrations from week 0 onwards in MC-0.00, MC-0.25, and MC-0.50 were stable throughout the experiment, ranging from 9.55 mg L^{-1} (MC-0.00) and 15.7 mg L^{-1} (MC-0.50). A positive trend between Mg concentrations and gypsum amendment rate was observed, with a similar graph profile as Ca.

Potassium concentrations in porewater ranged from 18.8 mg L^{-1} (MC-0.25, week 2) to 208 mg L^{-1} (MC-0.00, week 8) over the course of the experiment (Figure 3-3). K concentrations decreased slightly from week 0, which ranged between 23.9 mg L^{-1} (MC-0.50) and 62.8 mg L^{-1} (MC-0.25), to week 2, which ranged between 18.3 mg L^{-1} (MC-0.25) and 36.8 mg L^{-1} (MC-0.00).

After remaining relatively stable for week 4, K concentrations increased for week 8, ranging from 58.6 mg L^{-1} (MC-2.00) to 209 mg L^{-1} (MC-0.00). Concentrations then steadily decreased to week 64, ending with a range between 39.5 mg L^{-1} (MC-1.00) and 64.9 mg L^{-1} (MC-0.00). The control batch had the highest K concentration, while the other batches had no obvious trends between differing gypsum amendments.

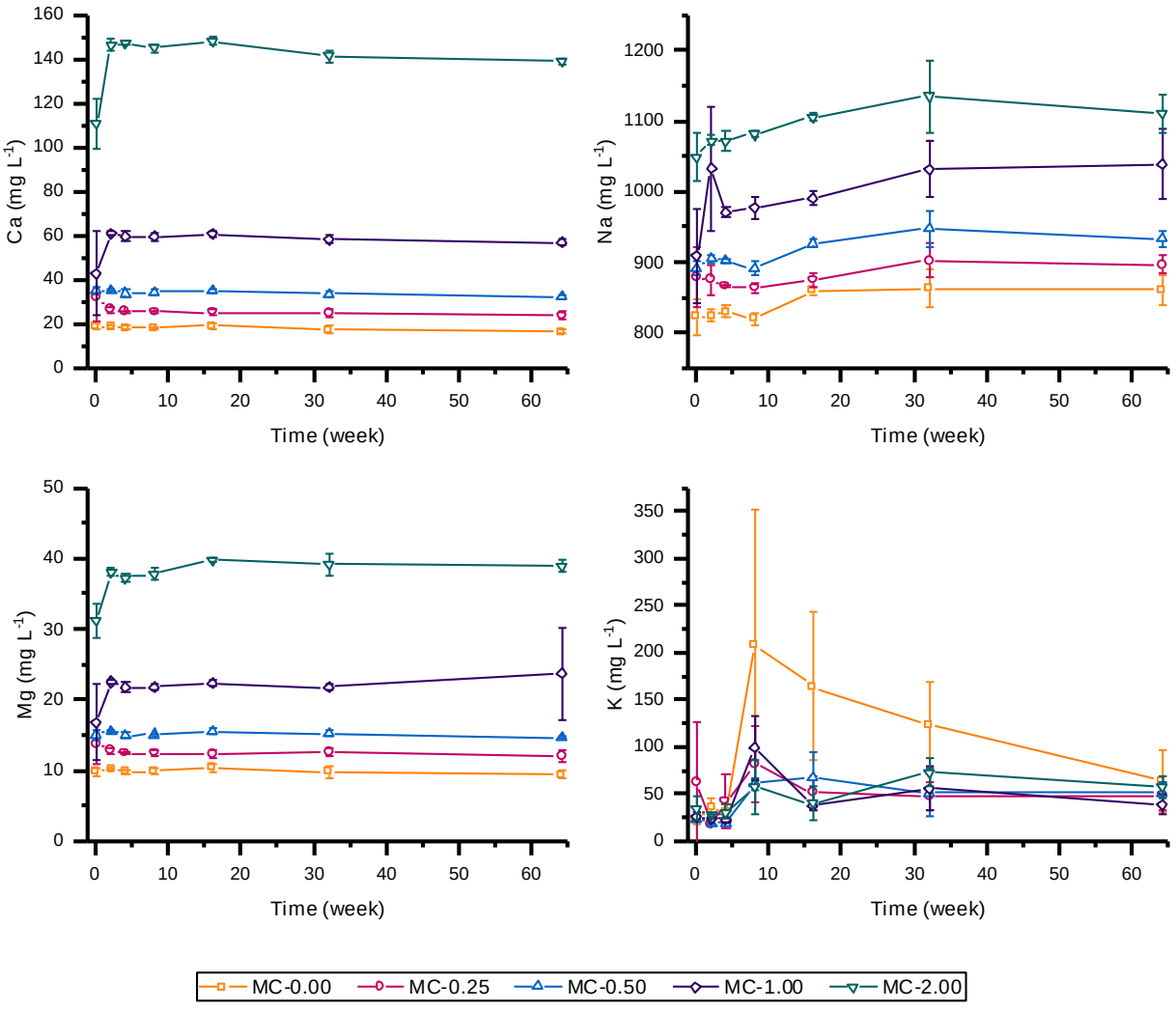

Figure 3-3: Porewater sodium (mg L^{-1}), calcium (mg L^{-1}), magnesium (mg L^{-1}), and potassium (mg L^{-1}) for the batch experiment. Error bars are one standard deviation.

3.5.2.3 Total Sulfide, Sulfate, Sulfur, and Iron

Dissolved ΣH_2S concentrations ranged from 26.8 µg L^{-1} (MC-2.00, week 4) to 235 µg L^{-1} (MC-0.00, week 64) over the course of the experiment (Figure 3-4). Week 0 ΣH_2S concentrations ranged between 30.1 µg L^{-1} (MC-2.00) and 86.0 µg L^{-1} (MC-0.50), and generally increased to week 32, ranging from 42.9 µg L^{-1} (MC-1.00) to 109.2 µg L^{-1} (MC-0.00). Concentrations increased higher for week 64, ending between 141 µg L^{-1} (MC-2.00) and 235 µg L^{-1} (MC-0.00). In general, there was an inverse trend between the concentration of ΣH_2S and increasing gypsum amendment rates, especially from week 16 to the end of the experiment.

Total SO_4 concentrations in porewater ranged from 44.9 mg L^{-1} (MC-0.00, week 64) to 1440 mg L^{-1} (MC-2.00, week 8) during the experiment (Figure 3-4). SO_4 concentrations exhibited an initial increase from week 0, which ranged from 100 mg L^{-1} (MC-0.00) to 1040 mg L^{-1} (MC-2.00), to week 2, which ranged from 141 mg L^{-1} (MC-0.00) to 1430 mg L^{-1} (MC-2.00), with the largest increases corresponding to larger gypsum amendments (MC-1.00 and MC-2.00). Concentrations decreased between weeks 2 and 64, with final concentrations ranging from 44.9 mg L^{-1} (MC-0.00) to 1343 mg L^{-1} (MC-2.00). There was a positive trend between the gypsum amendment rates and the concentration of porewater SO_4.

Total S concentrations in porewater ranged from 25.3 mg L^{-1} (MC-0.00, week 64) to 559 mg L^{-1} (MC-2.00, week 32) over the course of the experiment (Figure 3-4). Total S concentrations exhibited an initial increase from week 0, which ranged from 35.8 mg L^{-1} (MC-0.00) to 351 mg L^{-1} (MC-2.00), to week 2, which ranged from 51.5 mg L^{-1} (MC-0.00) to 482 mg L^{-1} (MC-2.00), with the largest increases corresponding to larger gypsum amendments (MC-1.00 and MC-2.00). Total S concentrations remained steady between weeks 2 and 64 for all

amendments, except for MC-2.00, which increased in week 32. A positive trend between total S concentrations and gypsum amendment rates was observed.

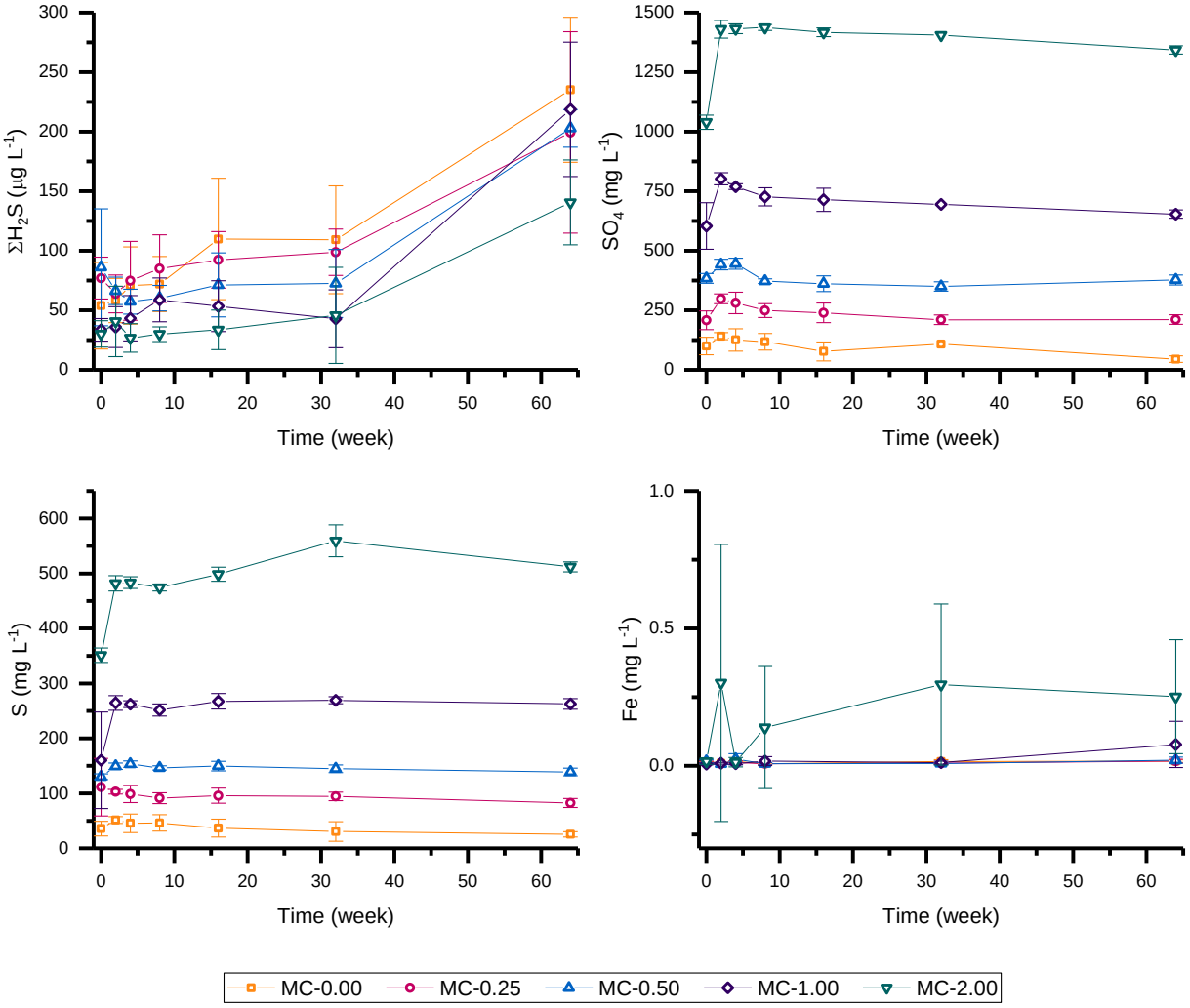

Figure 3-4: Porewater sulfide (µg L^{-1}), sulfate (mg L^{-1}), sulfur (mg L^{-1}), and iron (mg L^{-1}) for the batch experiment. Error bars are one standard deviation.

Iron concentrations in porewater ranged from 6.53 x10^{-3} mg L^{-1} (MC-1.00, week 0) to 0.30 mg L^{-1} (MC-2.00, week 2) over the course of the experiment (Figure 3-4). Concentrations were relatively stable for all concentrations, except for MC-2.00, which increased from week 0 (0.016 mg L^{-1}) to week 2 (0.30 mg L^{-1}), decreased for week 4 (0.013 mg L^{-1}), and increased for

week 8 (0.14 mg L^{-1}) to 64 (0.25 mg L^{-1}). Overall, the highest porewater Fe concentrations were observed in the highest gypsum amendment rate.

3.6. DISCUSSION

Hydrocarbon degradation by anaerobic microbes can produce CO_2 and CH_4 (Das and Chandran, 2011; Siddique et al., 2014; Dompierre et al., 2016). Although CH_4 production was observed in all batches, distinct difference between treatments and the control were not apparent. Increased CH_4 concentrations from the gypsum amendments were not observed, and therefore I am unable to determine whether the gypsum addition influenced methane production. Other studies have shown that SRB and methanogens can co-exist, however the presence of excess sulfate inhibits methanogenesis (Ramos-Padrón et al., 2011; Heaton, 2015; Rudderham, 2019). Although not a principal goal for gypsum amendment in FFT, if sulfate addition could supress methanogenesis, that would be a positive outcome. It is still unknown how differing concentrations of gypsum impacts methane production.

Dissolved CO_2 concentrations remained relatively constant after week 8, which may indicate a decline of labile organic carbon compounds or similar rates of gas production and consumption. Hydration of CO_2 forms carbonic acid (H_2CO_3; Equation 3.1), which releases H^+ when it dissociates (pKa = ~6.35) (Equation 3.2; Siddique et al., 2014).

$$CO_2 + H_2O \rightarrow H_2CO_3 \qquad \text{Equation 3.1}$$

$$H_2CO_3 \rightleftharpoons HCO_3^- + H^+ \qquad \text{Equation 3.2}$$

Following the initial decrease of porewater pH, which is attributed to increased dissolved CO_2 concentrations, values were relatively stable. The pH remained mildly alkaline between 7.6 and 8.1 throughout the batch experiments.

The alkalinity decrease observed between week 0 and 4 likely results from a pH decrease associated with CO_2 generation and hydration followed by $H_2CO_3^0$ dissociation (Equations 3.1 and 3.2). Although HCO_3^- contributes to alkalinity, dissociation of $H_2CO_3^0$ (Equation 3.2) generates protons and does not directly increase alkalinity; these protons promote the dissolution of carbonates (calcite, dolomite, etc.). The CO_3^{2-} produced by this reaction subsequently protonates to form HCO_3^- (Equation 3.3). This process is likely responsible for observed alkalinity increases after week 4.

$$CaCO_3 + H^+ \rightleftharpoons HCO_3^- + Ca^+ \qquad \text{Equation 3.3}$$

Carbonate dissolution with decreasing pH creates an increase in cations (e.g., Ca and Mg) in the porewater (Siddique et al., 2014; Dompierre et al., 2016). Magnesium is less likely to be exchanged in reactions compared to Ca, and Mg sulfates (e.g., dolomite; Dompierre et al., 2016) exhibit greater solubility than Ca sulfates (e.g., gypsum). The dissolution of Ca and Mg-bearing carbonates would lead to a relative increase in Mg compared to Ca; however, the Ca concentration in FFT porewater is bolstered by gypsum amendment. With increasing divalent cation concentrations in the porewater, the EDL thickness decreases from cation exchange of dissolved Ca^{2+} for sorbed Na^+, leading to increased Na concentrations in FFT porewater. This exchange reaction has reached an apparent steady state within the first two weeks of the experiment, as concentrations of Ca and Na are relatively stable after week 2, once a maximum cation exchange on the clay minerals in the FFT has been reached. There was a slight increase in K concentrations, most likely due to exchange reactions.

Measured Eh values were not representative of the anoxic environment in the batches. Eh values ranged from 210 to 430 mV (average = 315 mV), which is higher than theoretical anoxic Eh values (+40 < Eh < -350 mV; Markelova et al., 2017). Inconsistencies could be due to the

presence of microbial exudates produced under reducing conditions (Markelova et al., 2017). In other anoxic lab-based studies Eh values were approximately −200 mV in FFT porewater (Chen et al., 2013). Other parameters indicate the batches were anoxic, including the presence of CH_4 in the headspace from methanogenesis and H_2S in solution from SO_4 reduction.

With the increasing addition and dissolution of gypsum in the FFT, the concentrations of SO_4 and total S increased. Once the gypsum was dissolved after week 2, the total S concentrations exhibited little variation. Mass balance for total S often did not equal to SO_4 and ΣH_2S, with most cases having a higher total S concentration. This suggests the presence of intermediate or secondary sulfur species that were not analyzed, such as iron sulfides or thiosulfate (Stasik et al., 2014). The overall decrease of SO_4 concentration between weeks 2 to 64 among all treatments suggests sulfate reduction was occurring, with possible formation of intermediate sulfur species. With increasing gypsum amendment, the total S concentration increases, while the concentration of ΣH_2S was lower. The lack of ΣH_2S in the porewater may be due to metal sulfide precipitation, which may also serve as a control for Fe concentrations in the porewater (Ramos-Padrón et al., 2011). Although Fe concentrations are generally low, the batches with the two highest gypsum amendments exhibited a slight increase in Fe concentrations after week 4 (MC-2.00) and week 32 (MC-1.00), which is likely dominated by Fe^{2+} due to the thermodynamically favored reduction dissolution of Fe^{3+} (Dompierre et al., 2016). An excess of Fe^{2+} limits ΣH_2S accumulation, and vice versa, through the precipitation of Fe(II) sulfides (Heaton, 2015; Foght et al., 2017).

Results were inconclusive on whether the gypsum addition influenced methane production. However, gypsum addition was shown to increase the concentration of dissolved Na^+ in the porewater, due to the excess Ca^{2+} in the system. This increase in dissolved salt in FFT may pose

challenges during reclamation. There needs to be a balance between beneficial gypsum addition to FFT in terms of consolidation, but not in excess to reduce salinization of porewater and surface reclamation water during closure.

CHAPTER 4: COLUMN EXPERIMENT

The impacts of successive freeze-thaw-evaporation cycles on porewater chemistry within CFT deposits are not fully understood. Therefore, laboratory column experiments were conducted to examine how such cycles alter the porewater chemistry with particular focus on the redistribution of dissolved salts. Column experiment results contribute new information on the magnitude of change in dissolved salt concentrations within CFT pore water, and offer insight into the potential for salt migration into overlying reclamation soil covers placed on CFT deposits previously subjected to freeze-thaw-evaporation cycles. These findings will help inform ongoing development of mine closure strategies for CFT and other treated tailings materials generated at oil sands mining operations.

4.1. EXPERIMENTAL SETUP

Six columns were constructed for this experiment from non-corrugated polyvinyl chloride (PVC) pipe with custom PVC caps (Figure 4-1). The pipes had an inner diameter of 36.5 cm and internal length of 90 cm. At this width, wall effects from the side of the columns would be minimized and top to bottom freezing and thawing would be promoted. The height was at least double the width, allowing for movement of salts within the columns. The bottoms were capped, and the column walls and bottom were insulated to promote top-down freezing and thawing. The column outer walls were wrapped with fiberglass insulation (R20) and sealed with aluminized non-stretch polyester film. Two-inch thick rigid foam (R10) was placed at the inner base of each column, and reported dimensions were measured from the top of the foam layer.

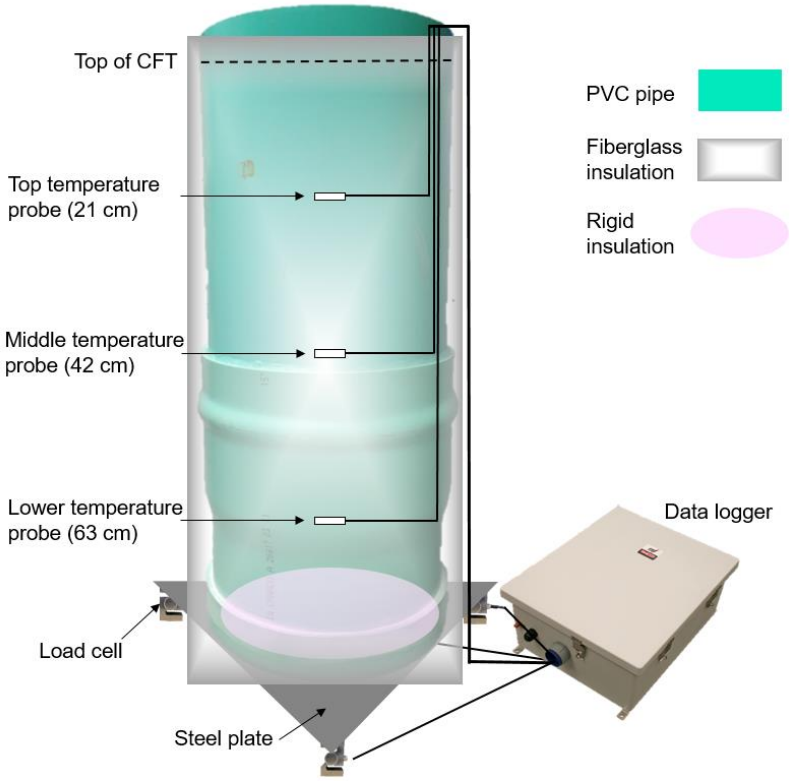

Figure 4-1: Individual column set-up showing placement of insulation, temperature probes, and load cells.

Columns were centered on triangular 1.6 cm (5/8 in) steel plates with one load cell (Model 127, S-type, Hoskin Scientific) positioned at each corner (Figure 4-1, Figure 4-2). The load cells had a capacity of 100 kg, with a precision of ± 0.03%, and were utilized to monitor changes in column mass during the experiment. Calibration curves were developed for each cell by applying increasing loads (n = 6) with a high-precision load frame (HM-5030 Master Loader, Humboldt Mfg. Co.). Temperature sensors (109 AM-L, Campbell Scientific) were used to monitor *in situ* temperatures at three positions within each column. These sensors were installed during filling at distances of 21, 42 and 63 cm below the initial CFT surface. The load cells and temperature probes were connected to a data logger (CR1000X, Campbell Scientific) with two channel-relay multiplexers (AM16/32B, Campbell Scientific), and 24.9 kΩ 0.1% resistors. Power was supplied

by a 12 V battery (Campbell Scientific, PS150, USA) that remained connected to a power source throughout the experiment. The data logger was programmed to record measurements at 30-min intervals. Air temperature in the chamber was recorded with an external temperature sensor.

4.2. CENTRIFUGED FINE TAILINGS

Freshly prepared CFT samples, treated with gypsum and anionic polyacrylamide, were collected in October, 2017, from a commercial-scale centrifuge plant located at the Mildred Lake mine operated by Syncrude Canada Ltd. The FFT used to produce this CFT was collected from South West Sand Storage, a 25 km^2 tailings ponds located about 35 km northwest of Fort McMurray, Alberta (Booterbaugh et al., 2015). In total, 627 L was collected into 33 pails that were immediately sealed and shipped to the University of Saskatchewan, where they were stored at ambient laboratory temperature (~22 ^oC) until the experiment was initiated.

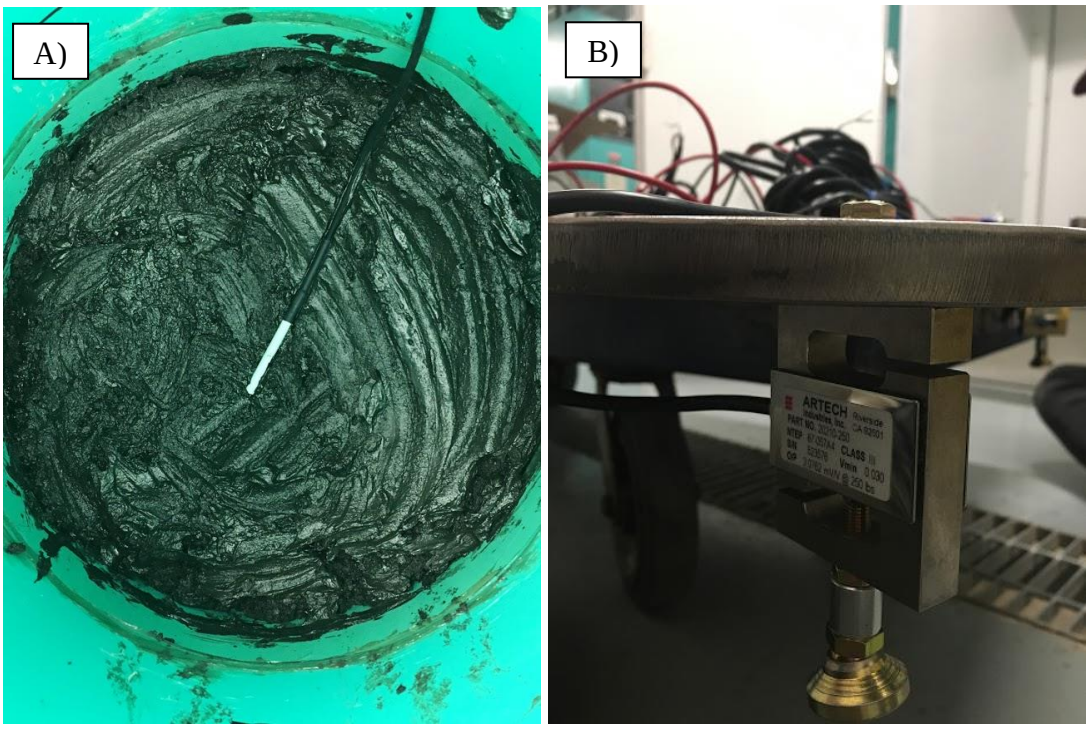

Figure 4-2: A) A bottom (63 cm) temperature probe in the middle of a column, on top of levelled CFT. B) A load cell attached to the bottom of a triangular steel plate.

Initial release water was decanted from the CFT surface, and initial samples of both CFT and release water from each pail were retained for analysis. These water samples are referred to as "initial porewater". The CFT within each pail was homogenized by inverting each pail a minimum of ten times, and individual pails were randomly selected to fill the columns. The CFT was transferred into the columns using a small shovel with care taken to ensure even distribution over the column area to avoid creating entrained air pockets. At predetermined positions above the column bottom (i.e., 21, 42, and 63 cm), the CFT was levelled and a temperature probe was installed (Figure 4-2). These probes were positioned in the middle of the columns and the wire was taped with slack to the inside column wall to allow wire movement during CFT settlement and dewatering. The columns were filled to a final height of 84 cm above the column base.

4.3. EXPERIMENTAL CONDITIONS

The column experiments were conducted in an environmental chamber located at the Controlled Environment Facility in the Department of Agriculture and Bioresources at the University of Saskatchewan. The chamber (Conviron PGV36, Controlled Environments Ltd.) is 2.44 m (96 in) tall, 3.34 m^2 (36 ft^2), and has a controlled temperature range of −10 to 45 ºC (±0.5 ºC) with a maximum relative humidity (RH) of 95 % at 30 ºC. Columns were positioned around the data logger and other instrumentation within the chamber (Figure 4-3).

Following column setup, the chamber air temperature was maintained at +25 ºC for 24 hours before starting the first freeze-thaw-evaporation cycle. Freezing was initiated by linearly decreasing the chamber air temperature from +25 to −2 ºC over 72 h and subsequently maintaining this temperature for 14 d. Cilia (2017) reported that the eutectic point for pore water within CFT deposits is likely between −1 and −2 ºC. Therefore, the initial 14 d freezing period at −2 ºC was selected to facilitate slow freezing and promote salt exclusion. After this period, the air temperature

was decreased linearly from −2 to −10 ºC over 48 h and maintained at this temperature until all *in situ* sensors recorded temperatures below −8 ºC for at least 72 h. The air temperature was then linearly increased from −10 to +25 ºC over 72 h to initiate thawing. Released porewater was drained during CFT thawing to mimic runoff that occurs in field deposits. The chamber was then maintained at a temperature of +25 ºC for 30 to 53 d to promote and maximize evaporation. This temperature cycle was repeated three times. Throughout the experiment RH within the chamber was set to 40%, the lowest average *in situ* RH to allow for a higher evaporation rate. Lights in the chamber were turned off during the freeze and thaw cycles to limit additional heat that would promote evaporation; the lights were turned on during evaporation cycles.

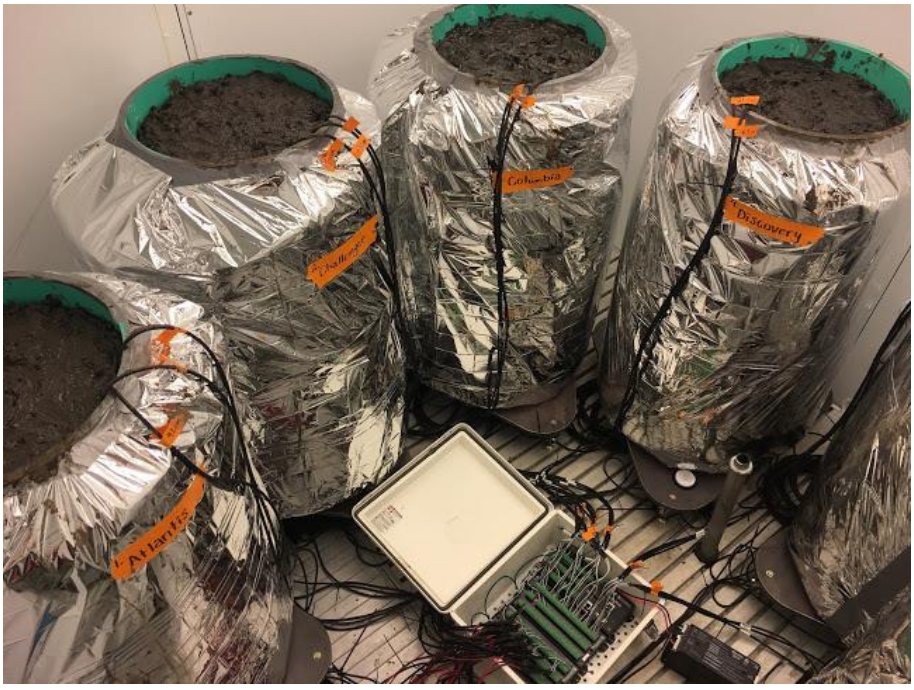

Figure 4-3: Six columns positioned around the data logger within the environmental chamber, at the beginning of the experiment.

4.4. COLUMN SAMPLING

All six columns were subjected to the first freeze period, and one column was sacrificially sampled at the end of each subsequent thaw period and evaporation period (Table 4-1). In total,

three freeze-thaw-evaporation cycles were performed with the sixth column sampled following the evaporation period of the third cycle. The second freeze period was extended due to battery failure in the data logger. Subsequent thawing and evaporation periods were shorter, due to the loss of water (and therefore quicker thawing), and increased efficiency during sampling.

Table 4-1: Gantt chart showing experimental duration for each column and timing of sacrificial sampling (✓) during sequential freeze (F), thaw (T) and evaporation (E) cycles (1, 2, 3).

Column #	Cycle ID (cycle duration)								
	F_1 (56 d)	T_1 (18 d)	E_1 (38 d)	F_2 (104 d)	T_2 (14 d)	E_2 (29 d)	F_3 (56 d)	T_3 (12 d)	E_3 (21 d)
1		✓							
2			✓						
3					✓				
4						✓			
5								✓	
6									✓

During sacrificial sampling, each column was sectioned into six discrete depth intervals and samples positioned within 5 cm of the inner column wall was discarded (Figure 4-4). The CFT was collected using clean wooden spoons, with the following partitions from the CFT surface, down: three 5 cm sections, two 10 cm sections, and one section with the remaining CFT (Figure 4-4). The first 5 cm section included any salt from the top; the thickness of the bottom interval varied among all columns to accommodate settlement (ranging from 23.0-26.5 cm) (Figure 4-4). Smaller sections at the top of the columns were used to capture more detail in potential changes in salt distribution due to water release and evaporation.

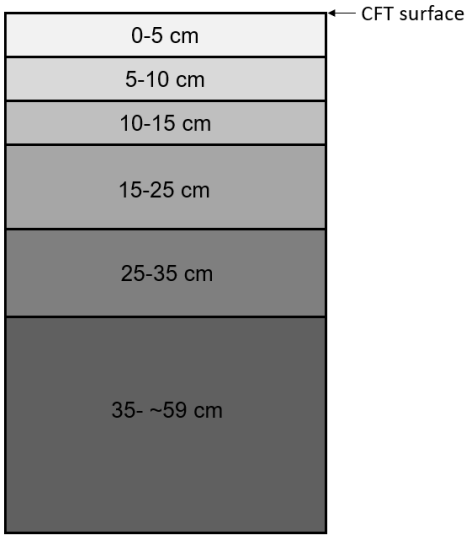

Figure 4-4: Individual columns were sectioned into six intervals during sampling.

CFT from a given interval was collected into a single container and mixed by hand, and subdivided into 250 mL centrifuge bottles (Thermo Scientific, 3141-0250). The samples were centrifuged (Beckman Coulter, Avanti J-E) at 10,000 rpm (15,800 g) for 45-60 min, with longer centrifuge times required for samples with lower water content. Extracted porewater was decanted into sterile polypropylene conical centrifuge tubes (50 mL; VWR, USA).

Porewater pH, redox potential (Eh), electrical conductivity (EC), hydrogen sulfide (ΣH_2S), ammonia (NH_3-N), and alkalinity were measured immediately after centrifugation. EC was measured on unfiltered porewater using conductivity cell (Thermo Orion, model 011050MD, USA) that was first calibrated to a 1,413 µS cm^{-1} standard. Additional measurements were performed on porewater that was first passed through 0.45 µm PES syringe filter membranes (Pall Corporation, USA) using sterile syringes (HSW GmbH, Germany). The pH electrode (Thermo Orion, model, 8156BNUWP, USA) was calibrated to NIST traceable pH 4, 7, and 10 buffer solutions. Performance of the Eh electrode (Thermo Orion, model 9678BNWP, USA) was checked against Zobell's (Nordstrom, 1977) and Light's (Light, 1972) solutions. Electrode performance was

rechecked between each measurement and recalibration was carried out as required. Dissolved ΣH_2S and NH_3-N concentrations using the methylene blue (Method 8131, Hach, USA) and salicylate (Method 10205, Hach, USA) spectrophotometric methods (DR 2800, Hach, USA). Alkalinity was determined by titration with a normalized sulfuric acid solution (Method 8203, Hach, USA) to the bromocresol green methyl red endpoint.

Porewater samples for inorganic anion (i.e., SO_4^{2-}, Cl^-) and major element (i.e., Na, Ca, Mg, K, S, Fe) quantification were passed through 0.45 µm or 0.2 µm filters, respectively, and stored in high density polyethylene (HDPE) bottles. The major element samples were acidified to pH < 2 with concentrated high-purity nitric acid (HNO_3; OmniTrace, EMD Millipore, USA). All samples were stored in the dark at 4 °C until analysis. Major element concentration were determined by inductively coupled plasma–optical emission spectroscopy (ICP–OES; EPA Method 200.7). Inorganic anion concentrations were determined by ion chromatography (IC; EPA Method 300.0).

4.5. RESULTS

4.5.1 Observations

Ice crystals formed on the top of each column during the first freezing cycle. After the first freeze-thaw process, the CFT surface elevation settled 23 cm in Column 1 and 22.5 cm in Column 2 due to settlement and dewatering. Precipitates were observed on the surface of the columns near the edges during the first thawing period, and extended to the center of the columns during the first evaporation period. These precipitates remained in all columns until sampling. CFT surfaces exhibited less ice crystal formation during the second freezing cycle, and CFT settled a cumulative 26 cm in Column 3 and 25 cm in Column 4. During the second freezing period, CFT at the top of all remaining columns exhibited desiccation cracks up to a depth of 8 cm. During the third freezing period, CFT began to pull away from the edges of the columns. Ice crystals were

only visible down the sides and did not form on the top of Columns 5 and 6. Following the final thawing period, CFT in Columns 5 and 6 settled a cumulative 26.5 cm and 27 cm, respectively.

4.5.2 Temperature and Load Cells

Temperatures within the columns ranged from −9.3 ºC (Columns 3 and 6) to 25.0 ºC (all columns) over the course of the experiment. Vertical temperature profiles within individual columns confirmed that freezing and thawing proceeded from top to bottom (Figure 4-5). During the first freezing period, the chamber reached −2 ºC on day 4; the lag times between the air temperature and the in-situ temperature sensors averaged 27 d (upper), 36 d (middle), and 37 d (lower). For the second freeze period, the chamber reached −2 ºC on day 115; the lag times between the air temperature and the temperature sensors averaged 23 d (upper) and 26 d (middle and lower). The third freeze period at the chamber reaching −2 ºC on day 262; the lag times between the air temperature and the temperature sensors averaged 22 d (upper), 25 d (middle), and 26 d (lower).

During the first thaw process, the chamber reached 0 ºC after 56 d. The lag times between the air temperature and temperature sensors was 6 d (upper), 9 d (middle), 10 d (lower). Although the upper temperature probes were the first to record a temperature increase, all temperature probes reached 20 ºC after 70 to 71 d. This top to bottom thawing pattern continued in the second thaw cycle; however, exact days of thawing was not recorded due to battery failure in the data logger. The third cycle had the chamber set temperature at 0 ºC after 315 d, and the lag times between the air temperature and the temperature sensors was 5 d (upper and middle), and 6 d (lower).

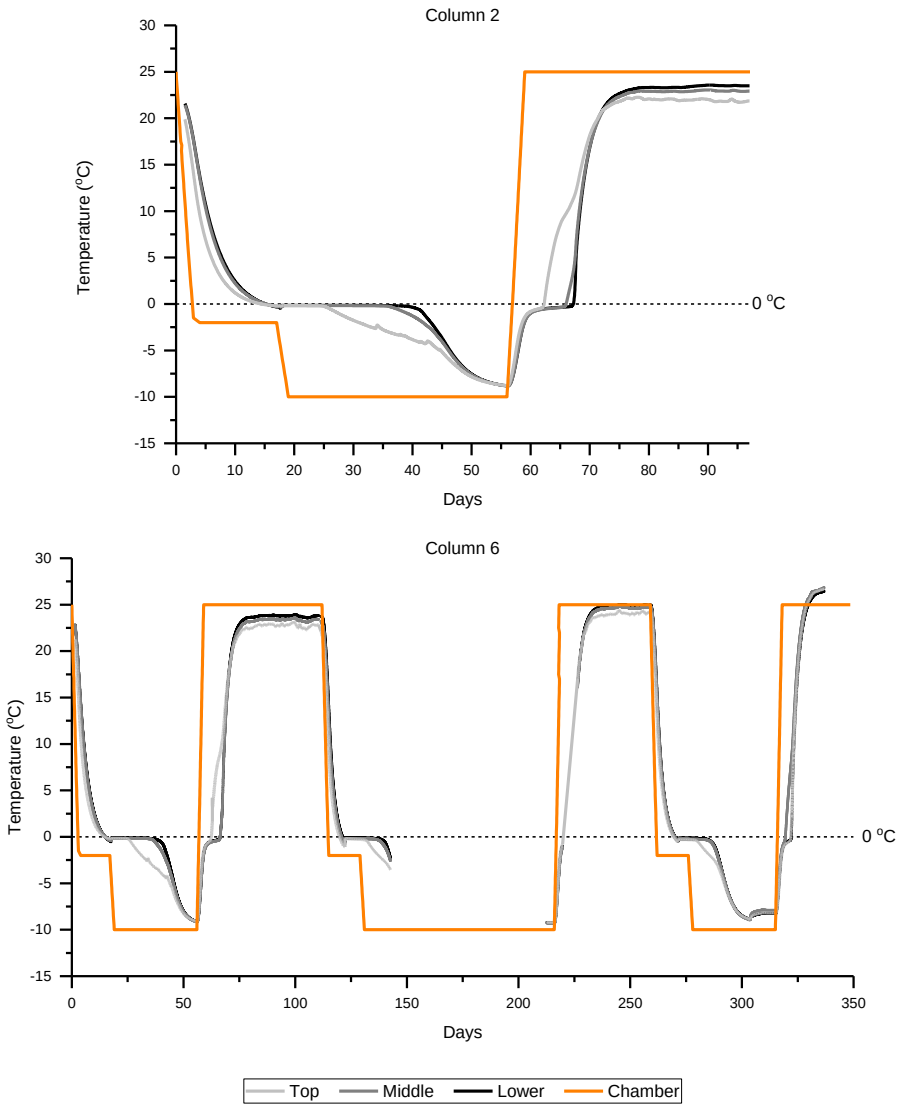

Figure 4-5: Temperature probes (upper, middle, and lower) in Columns 2 and 6 going through 1 and 3 freeze-thaw-evaporative cycles, respectively. Orange line is set temperature in the chamber.

Load cell measured masses were summed for each column for the entirety of the experiment, then all columns are shown in Figure 4-6. At the beginning of the experiment, the average weight of the six columns was 185.6 kg, which includes the column, cap, insulation, steel plate, CFT, and temperature probes. Column masses remained relatively constant during the first freeze period (56 d). During the first thaw period (18 d), the mass loss attributed to release water drainage averaged 20.5 kg among all columns (1.1 kg d^{-1}). During the first evaporation period (38 days),

an average mass loss of 6.4 kg was observed in the remaining columns (0.2 kg d^{-1}). Weight of each column remained relatively stable during the second freeze period (104 d). The second thaw period (14 d) showed consistent mass, and the second evaporative period (29 d) showed an average weight loss of 1.5 kg (27.7 g d^{-1}). The third and final freeze period (56 d) saw relatively stable weights in the remaining columns. The third thaw period (12 d) showed an average weight loss of 0.05 kg (4.2 g d^{-1}). Data was not collected during the final evaporative period (21 d), due to inadequate power supply. Evaporative water loss decreased during subsequent freeze-thaw-evaporative cycles. An additional evaporation experiment was conducted in the chamber, and determined that the rate of evaporation for free-standing OSPW from Syncrude Canada Ltd at 25 ^{o}C was 0.2 kg d^{-1}.

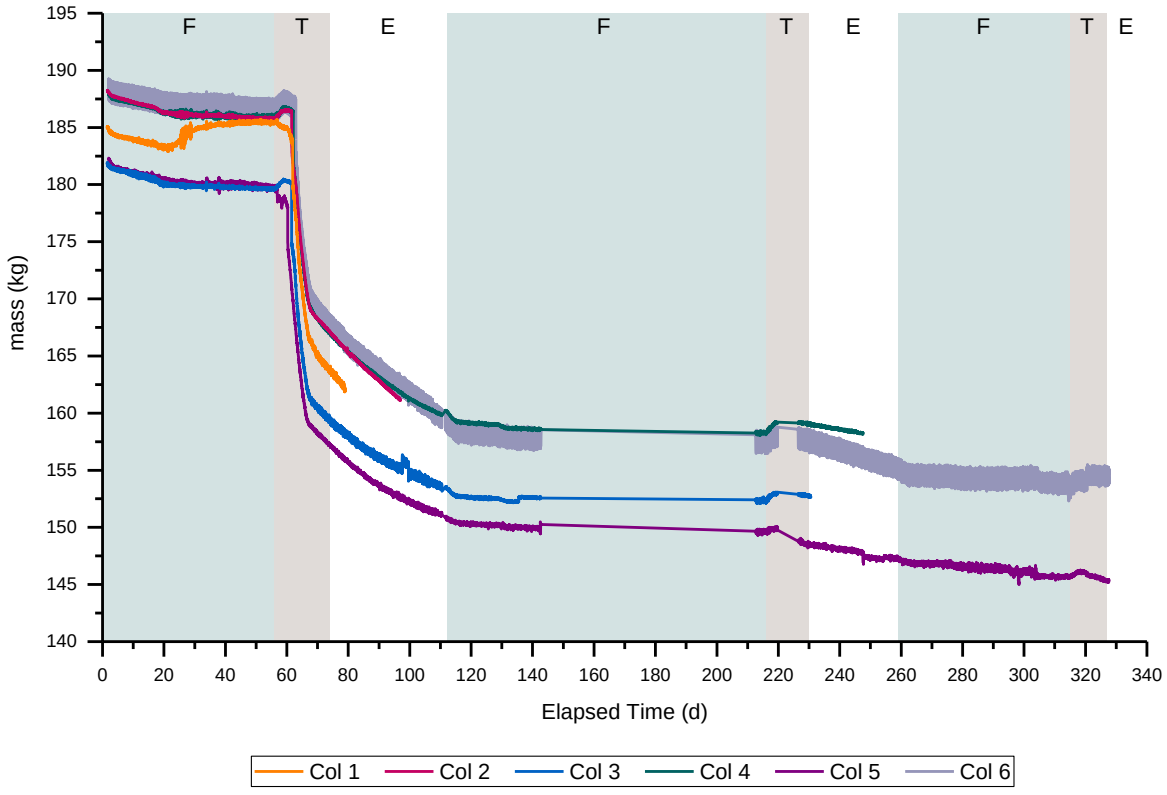

Figure 4-6: Mass of six columns plus steel plates, over the three Freeze (F), Thaw (T), and Evaporative (E) periods.

4.5.3 Porewater Chemistry

Porewater extraction was limited in samples collected from the uppermost depth interval(s) because of lower water content attributed to evaporative loss, and therefore not all columns have data for the samples at the top of the column. Porewater collected during the initial filling of the columns with CFT is referred to as "initial porewater," and porewater collected during each columns sampling time is referred to as "final porewater." Final porewater data was compared to averaged results from initial porewater.

4.5.3.1 pH, EC, Alkalinity, and Ammonia

The average pH was 7.6 (n = 21) for initial CFT porewater samples. (Figure 4-7). Final porewater pH remained lower than initial porewater for all columns, except the lowest section in Column 6. pH did not vary systematically during successive freeze-thaw-evaporative cycles. Lowest pH values were observed at a depth of 7.5 cm, with the lowest pH in Column 2 at 6.6. The lowest section typically exhibited the highest pH values, which ranged from 7.5 (Columns 2 and 3) to 7.9 (Column 6).

Initial porewater samples had an average electrical conductivity (EC) of 3.53 mS cm^{-1} (n = 21; Figure 4-7). Final porewater EC remained higher than initial porewater for all columns, except for the lowest section in Column 2 where EC was 3.33 mS cm^{-1}. The highest porewater EC values after sampling were consistently observed in the uppermost sampling interval and increases were observed between columns sampled before and after a given evaporation period. Highest EC values were observed in the top sections of Columns 1 to 4, ranging from 12.83 mS cm^{-1} (Column 3) to 15.99 mS cm^{-1} (Column 4). With underlying sampling intervals, EC remained consistently lower in all the columns, ranging from an average of 4.93 mS cm^{-1} (lowest sections) to 7.98 mS cm^{-1} (12.5 cm depth). EC values increased from before to after evaporation periods;

Column 1 had an EC of 13.2 mS cm^{-1} at a depth of 2.5 cm, while Column 2 had an EC of 15.97 mS cm^{-1} at the same depth; Column 3 had an EC of 12.83 mS cm^{-1} at a depth of 7.3 cm, while EC was 15.99 mS cm^{-1} at the same depth in Column 4.

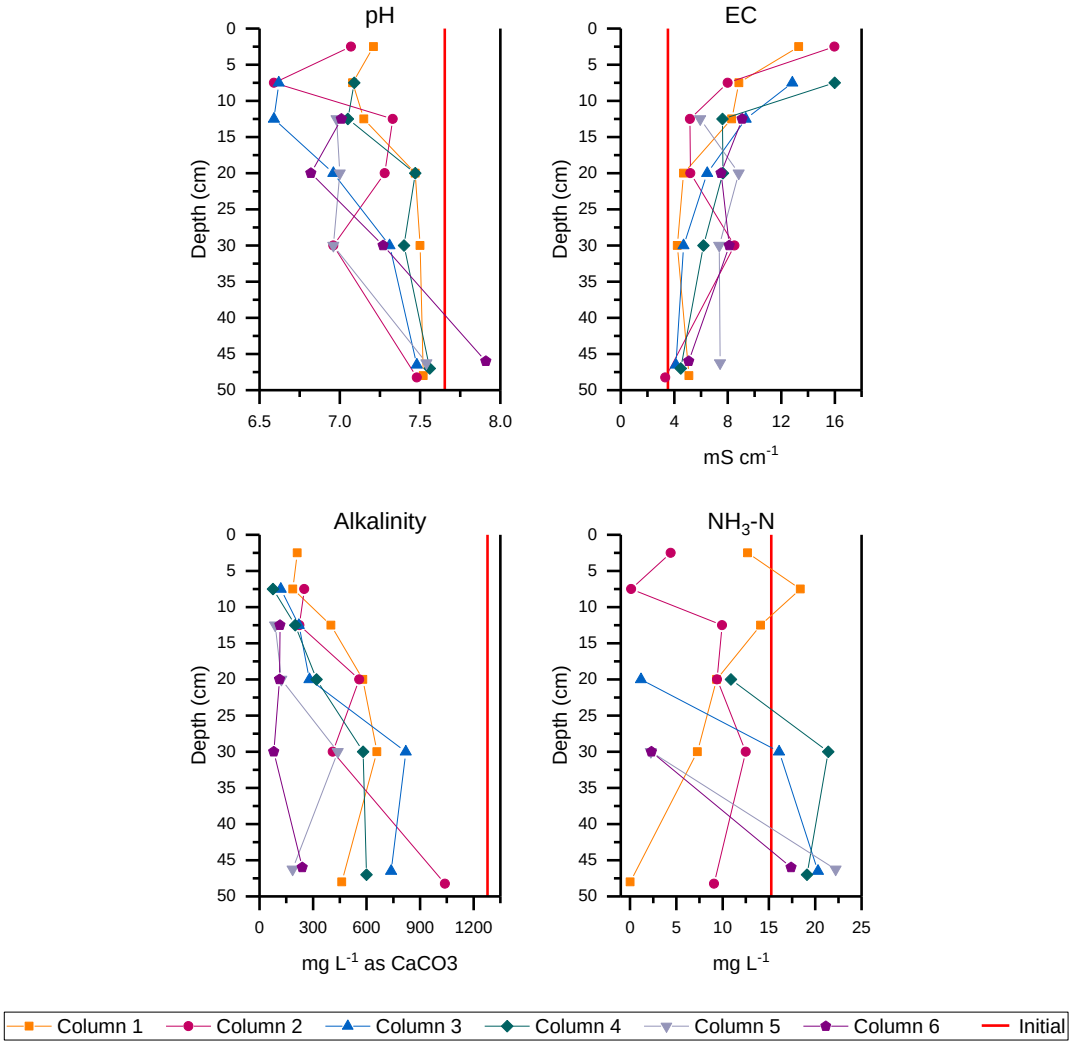

Figure 4-7: Depth profiles of porewater pH, electrical conductivity (mS cm^{-1}), alkalinity (mg L^{-1} as $CaCO_3$), and ammonia (mg L^{-1}). All depths normalized to CFT surface at time of sampling.

Initial porewater alkalinity (reported as $CaCO_3$ equivalents) averaged 1,270 mg L^{-1} (n = 21; Figure 4-7). Final porewater alkalinity values remained lower than initial porewater for all

columns. With successive freeze-thaw-evaporative cycles, porewater alkalinity generally decreased. The lowest alkalinity concentrations were observed in the uppermost sections of each column; at 12.5 cm depth, alkalinity concentrations were clustered with an average of 158.1 mg L^{-1} (Columns 1, 2, 3, and 4). The highest alkalinity concentrations were observed in the lowermost sections, ranging from 185.7 mg L^{-1} (Column 5) to 1,040 mg L^{-1} (Column 2).

Dissolved NH_3-N concentrations averaged 15.3 mg L^{-1} among initial CFT samples (n = 21; Figure 4-7). Final NH_3-N concentrations exhibited no consistent depth trends among columns, and there was no apparent distinction between freeze-thaw-evaporative cycles. Final porewater NH_3-N concentrations ranged from 0.017 mg L^{-1} (Column 1) to 22.2 mg L^{-1} (Column 5).

4.5.3.2 Major Cations and Chloride

Initial porewater had an average Ca concentration of 40.5 mg L^{-1} (n = 21; Figure 4-8). Final porewater Ca concentrations remained higher than initial porewater for all columns, except for the lowest section in Column 2 with a concentration of 40.1 mg L^{-1}. Ca concentrations did not vary systematically during successive freeze-thaw-evaporative cycles. Lowest concentrations were observed in the lowermost section of the columns, with an average of 152 mg L^{-1}.

Porewater Na concentrations averaged 772 mg L^{-1} for initial CFT samples (n = 21; Figure 4-8). Final porewater Na concentrations remained higher than initial porewater for all columns. The highest porewater Na concentrations after sampling were consistently observed in the uppermost sampling interval and increases were observed between columns sampled before and after a given evaporation period (Column 1 and 2). After a subsequent freeze-thaw-evaporative cycle, the porewater Na concentration in Column 3 peaked at a lower height compared to the first cycle. The highest Na concentrations were observed in the uppermost sampled sections in Columns 1, 2, and 3, ranging from 2,884 mg L^{-1} (Column 1) to 5,353 mg L^{-1} (Column 2). With underlying

sampling intervals, Na remained consistently lower in all the columns, ranging from an average of 1,006 mg L^{-1} (lowest sections) to 1,413 mg L^{-1} (12.5 cm depth). All columns decreased from the top to the bottom, with the biggest changes occurring near the top.

Initial porewater had an average Mg concentration of 22.0 mg L^{-1} (n = 21; Figure 4-8). Final porewater Mg concentrations remained higher than initial porewater for all columns, except for the lowest section in Column 2 with a concentration of 20.6 mg L^{-1}. The highest Mg concentrations were observed in the uppermost sampled section of each column, and there was no observed systematic change with successive freeze-thaw-evaporative cycles. Column 3 exhibited the highest porewater Mg concentration of 2,069 mg L^{-1} in the uppermost sampled section, and Mg concentrations within the upper 20 cm were elevated compared to the other columns. Excluding Column 3, the uppermost section in Columns 1 and 2 had an average Mg concentration of 446 mg L^{-1}. With underlying sampling intervals, Mg remained relatively consistent in all the columns, ranging from an average of 83.3 mg L^{-1} (lowest sections) to 236 mg L^{-1} (20 cm depth).

Initial porewater had an average K concentration of 16.1 mg L^{-1} (n = 21; Figure 4-8). Final porewater K concentrations remained higher than initial porewater for all columns, except for the lowest section in Column 2 with a concentration of 15.5 mg L^{-1}. With successive freeze-thaw-evaporative cycles, K concentration increases were observed between columns sampled before and after a given evaporation period (Column 1 and 2), and the concentrations peaked at a lower height. The highest K concentrations were observed in the uppermost sampled sections of Columns 2, 3, and 6, ranging from 179 mg L^{-1} (Column 3) to 251 mg L^{-1} (Column 6). Starting from 20 cm depth, underlying sampling intervals had relatively consistent K concentrations, with the lowest average K concentration (43.2 mg L^{-1}) occurring in the lowermost section of all columns. The uppermost section of Column 1 had a K concentration of 81.2 mg L^{-1},

and after the first evaporation period Column 2 had a concentration of 180 mg L^{-1} at the same depth. The lowermost samples also increased in average concentrations after successive freeze-thaw-evaporative cycles (Columns 1 and 2 average = 17.7 mg L^{-1}; Columns 3 and 4 average = 28.8 mg L^{-1}; Columns 5 and 6 average = 83.0 mg L^{-1}).

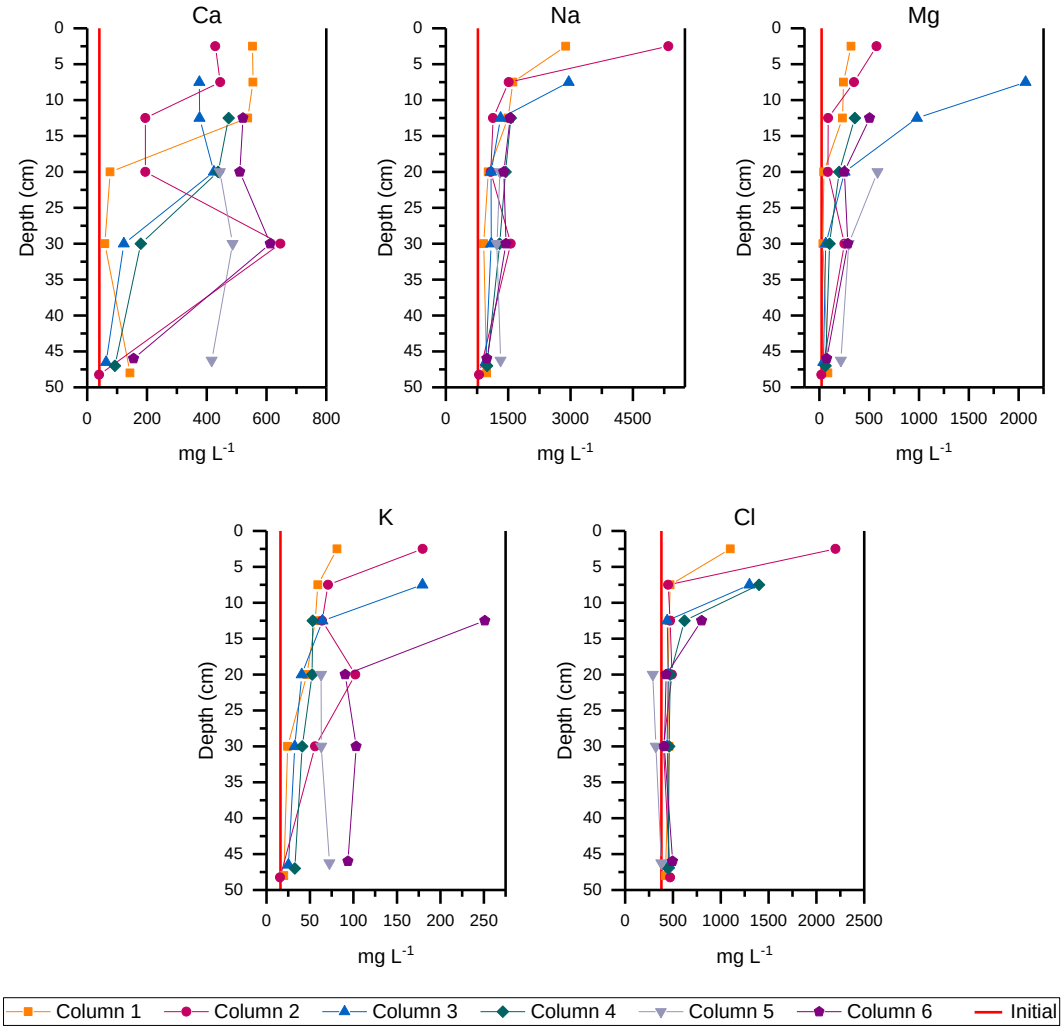

Figure 4-8: Depth profiles of porewater calcium (mg L^{-1}), sodium (mg L^{-1}), magnesium (mg L^{-1}), potassium (mg L^{-1}), and chloride (mg L^{-1}) concentrations for the column experiment. All depths normalized to CFT surface at time of sampling.

Initial porewater had an average Cl concentration of 379 mg L^{-1} (n = 21; Figure 4-9). Final Cl concentrations remained higher than initial porewater for all columns, except for the majority of Column 5. The highest porewater Cl concentrations after sampling were consistently observed

in the uppermost sampling interval and increases were observed between columns sampled before and after a given evaporation period. After a subsequent freeze-thaw-evaporative cycles, the Cl concentrations in Column 3 and 4 peaked at lower depths compared to the first cycle. The highest Cl concentration was observed in the uppermost sampled sections of Column 1, 2, 3, and 4, ranging from 1,100 mg L^{-1} (Column 1) to 2,200 mg L^{-1} (Column 2). With underlying sampling intervals, Cl remained consistently lower in all the columns, ranging from an average of 415 mg L^{-1} (30 cm depth) to 558 mg L^{-1} (12.5 cm depth). All columns decreased from the top to the bottom, with the biggest changes occurring near the top.

4.5.3.3 Total Sulfide, Sulfate, and Iron

Initial porewater had an average dissolved ΣH_2S concentration of 9.2 µg L^{-1} (n = 21; Figure 4-7). Final porewater ΣH_2S concentrations remained lower than initial porewater for all columns, except for Column 5 at 30 cm depth, where ΣH_2S was 10.6 µg L^{-1}. During individual freeze-thaw-evaporative cycles, the lowest column-averaged ΣH_2S concentrations followed the evaporation period. Dissolved ΣH_2S concentrations were generally lower during the second freeze-thaw-evaporation cycle relative to the first cycle. However, dissolved ΣH_2S concentrations measured during the third cycle were higher than those measured during both the first and second cycles. Highest ΣH_2S concentrations were observed at 20 cm depth (average = 7.4 µg L^{-1}); lowest concentrations were observed at 12.5 cm depth (Columns 1, 2, 3, 4 average = 2.3 µg L^{-1}) and in the lowest section (average = 3.2 µg L^{-1}).

Initial porewater had an average SO_4 concentration of 135 mg L^{-1} (n = 21; Figure 4-9). Final porewater SO_4 concentrations remained higher than initial porewater for all columns. The highest porewater SO_4 concentrations after sampling were consistently observed in the uppermost sampling interval. After a subsequent freeze-thaw-evaporative cycle, the SO_4 concentrations in

Columns 3 and 4 peaked at greater depths compared to the first cycle. The highest SO_4 concentrations were observed in the uppermost sampled sections of Columns 1, 2, 3, and 4, ranging from 7,200 mg L^{-1} (Column 1) to 1,4000 mg L^{-1} (Column 3). With underlying sampling intervals, SO_4 concentrations generally increased from before to after evaporation periods, and with subsequent freeze-thaw-evaporative cycles. In the lowermost sampling section, the average concentration increased from the previous cycle (Columns 1 and 2 average = 935 mg L^{-1}; Columns 3 and 4 average = 1,400 mg L^{-1}; Columns 5 and 6 average = 2,830 mg L^{-1}).

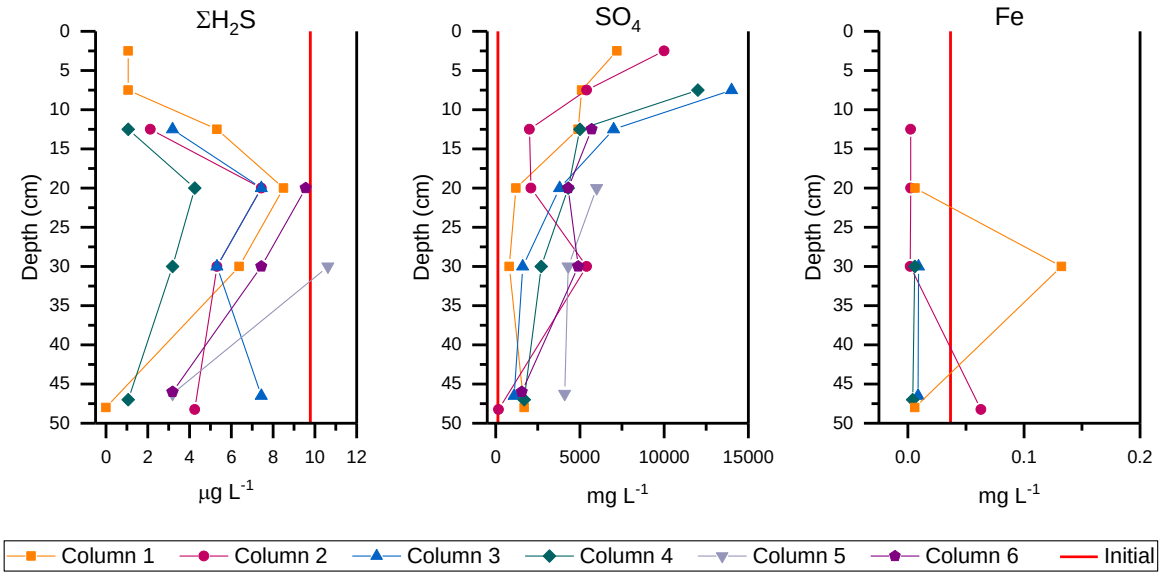

Figure 4-9: Depth profiles of porewater total sulfide (µg L^{-1}), sulfate (mg L^{-1}), and iron (mg L^{-1}) concentrations for the column experiment. All depths normalized to CFT surface at time of sampling.

Initial porewater had an average total Fe concentration of 0.037 mg L^{-1} (n = 21; Figure 4-8). Although concentrations are low, it appears that subsequent freeze-thaw-evaporative cycles reduces the concentration of total Fe in the columns. Only two samples had concentrations higher than the initial average: Column 1 at 30 cm depth (0.130 mg L^{-1}) and Column 2 in the lowermost section (0.063 mg L^{-1}). Columns 3 and 4 remained below the initial concentration averages. The

upper two to three samples in Columns 1, 2, 3, and 4, as well as all of Columns 5 and 6 had total Fe concentrations under detection limits.

4.6. DISCUSSION

Distinct temperature differences for the three temperature probes in all columns were observed following temperature changes in the chamber. The upper temperature probe (21 cm) responded quicker to set chamber temperature changes compared to the middle temperature probe (42 cm), which in turn responded quicker than the bottom probe (63 cm). This pattern confirms the freezing and thawing processes occurred from the top down, which is consistent with CFT deposits (Heaton, 2015).

The lag times in the CFT freezing and thawing periods decreased with subsequent freeze-thaw-evaporative cycles. In addition to the natural thermal gradient in the CFT from convection and conduction, the temperature lag between the lower and upper probes is due to variability in CFT thermal properties and a decrease in spacing between the temperature probes. CFT at shallower depths was exposed to the chamber temperature changes first, due to the open tops of the insulated columns, and allowed for a greater extent of evaporation at the top of the columns. During the first freeze and thaw periods, CFT at the bottom of the columns was water-saturated, and therefore less susceptible to temperature changes due to the high specific heat capacity of water (Cilia, 2017). Water content is the most influential factor in the CFT temperature, both in the column experiment and in the field (Heaton, 2015; Cilia, 2017). After subsequent freeze-thaw-evaporative cycles, a combination of decreased pore space due to the loss of water, and a decreasing distance between temperature sensors as the CFT dewaters and settles results in a smaller temperature lag between the lower temperature probes and the upper probes (Figure 4-5).

Differences between the initial average weights of the columns is attributed to slight differences in column, plate, and CFT masses. Column masses remained constant during the first freezing period because the lack of liquid water prevented evaporation and drainage. Following a rapid initial rate of mass loss associated with release water drainage during the first thawing period (2.2 kg d^{-1}), the mass loss rate declined approximately one-tenth (0.2 kg d^{-1}) during the subsequent evaporation period. The mass loss rate during the first evaporation period (0.2 kg d^{-1}) was consistent with results from a standing water evaporation experiment conducted in parallel with the column experiments. Declining rates of mass loss during the second and third thaw and evaporation periods are attributed to lower water content in the upper CFT. Rapid decreases in column masses during the first thaw period correspond to rapid release water drainage. In CFT deposits, each layer is subjected to one freeze-thaw-evaporation cycle before additional layers are deposited, promoting water loss via surface drainage and consolidation (Heaton, 2015). The design of the deposits is critical to facilitate proper surface drainage, as release water needs to flow away from the deposits.

After the first thaw period, evaporation is the major driver of mass loss. An average 6.4 kg of water was removed from the columns during the first evaporation period, and mass loss averaged 1.4 kg during the second evaporation period. The magnitude of evaporative water loss decreased due to the drying of the columns after additional cycles.

Evaporation concentrated dissolved salts in the CFT porewater and promoted precipitation of efflorescent salts at the surface. This evapoconcentration is apparent from depth profiles of dissolved Cl. Assuming Cl behaves conservatively in CFT porewater, the increased concentrations at the top of the columns represents the influence of evaporation. Similar Cl profiles were reported by Heaton (2015) in the study of experimental CFT deposits. Other major salts (Na, K, and SO_4)

exhibited similar concentration decreases, with the greatest change observed over the upper 20 cm of CFT within each columns. Concentration depth profiles for these major ions exhibit positive correlations, suggesting precipitation-dissolution and ion exchange reactions had limited influence on the major ion chemistry of CFT porewater. Consistent with Na, K, Cl and SO_4, porewater EC exhibited maximum values near the CFT surface and increased over successive freeze-thaw-evaporation cycles. High concentrations of dissolved salt poses challenges to reclamation and the ability to successfully grow flora (Carey, 2008; Li et al., 2014; Cilia, 2017; Simhayov et al., 2017; Lindsay et al., 2019; Vessey et al., 2019).

In contrast to Cl, dissolved Ca and Mg concentrations exhibited a gradual decreasing trend with depth below CFT surface. These differing trends are attributed to mass transfer reactions that influence dissolved Ca and Mg concentrations but not Cl or other more conservative constituents. For example, dissolved Ca^{2+} and Mg^{2+} can exchange for Na^{+} at clay-mineral surfaces with oil sands FFT and CFT deposits (Brown et al., 2013; Siddique et al., 2014; Heaton, 2015; Dompierre et al., 2016). Near the top of the columns, porewater Mg concentrations were elevated compared to Ca concentrations. This difference may result from multiple processes: (i) Ca sulfates are generally less soluble than Mg sulfates and may precipitate first during evapoconcentration; and (ii) Ca^{2+} more readily exchanges for Na^{+} at clay mineral surfaces than Mg^{2+} (Henry, 2010; Israelachvili, 2011). Evaporative precipitates on the surface of the columns likely contain Ca and Mg sulfates, thereby reducing the dissolved concentrations in porewater.

The pH remains circumneutral throughout the columns, ranging from a minimum of 6.59 near the top to a maximum of 7.91 in the lowest sections. The slight change in pH is attributed to anaerobic processes that produce CO_2 including Fe reduction, SO_4 reduction, and methanogenesis, which Heaton (2015) previously observed in CFT deposits. Alkalinity is consistent with pH,

generally increasing with depth in the columns. The dominant species in NH_3-N was NH_4^+ over the pH range observed in the experiment. Although the processes controlling NH_3-N concentrations are unclear, the variability with depth over time could be related to ion exchange reactions or the oxidation of NH_3-N, which may be enhanced near the top of the columns due to increased oxygen availability (Dompierre et al., 2016; Cilia, 2017).

During individual freeze-thaw-evaporative cycles, the lowest column-averaged ΣH_2S concentrations followed the evaporation period, likely due to an increase in microbial sulfate reduction during the warmer temperatures. Sampling of CFT in the field by Heaton (2015) found the highest ΣH_2S concentrations were reached at approximately 0.5 m below the surface. Sulfide concentrations in the columns had a similar profile, reaching maximum concentrations at 20 cm below the surface. Although dissolved Fe concentrations were generally below method detection limits, or near 0 mg L^{-1}, there were slight increases at depth in columns 1 and 2. This may be due to relative availability of Fe and ΣH_2S, where Fe only occurs with lower ΣH_2S, or due to carbonate dissolution.

Results show that the first thaw period accounts for the majority of water loss, and an average loss of 50 % of Na and Ca in the porewater, leading to potential for salt loading after the first freeze-thaw-evaporative cycle. After the first cycle, a decrease in rate of settlement and water content may lead to diffusion dominated salt migration. Salt release from CFT has the potential to migrate and accumulate in a reclamation setting, which can impact receptors such as vegetation and wetland water quality. This will potentially create issues during mine closure and reclamation. Including a capillary break to help prevent salt migration into overly reclamation covers, will help minimize the effect of salt at the surface (Cilia, 2017). Closure landscape design is important in terrestrial reclamation plans using CFT, in order to mitigate salt migration risks.

CHAPTER 5: Conclusions

The overall goal of this research was to assess the long-term effects of gypsum amendment to oil sands tailings (FFT and CFT), in preparation for mine closure. The laboratory batch experiment was conducted to understand the effect of gypsum-amended FFT, with two objectives: 1) examine temporal and spatial changes in porewater chemistry, and 2) assess temporal changes in carbon dioxide and methane production. Differing gypsum amendments were added to FFT, and destructively sampled over 64 weeks. Samples of the headspace gas were analyzed on a gas chromatograph, and water samples were analyzed for basic water chemistry, major anions, and major cations. Over the experimental duration, extensive methane production was not observed in the control, therefore, results were inconclusive on the effect gypsum addition had on methanogenesis. However, the experimental results showed an increase in salt (Na^+) in FFT porewater after gypsum-amendment, compared to the control. This will affect long-term water quality in aquatic technologies, and porewater and soil quality in terrestrial technologies using FFT. The rate of gypsum amendment needs to balance the benefit of consolidation without releasing excess salt.

The column experiment was conducted to determine the temporal changes in salt distribution in CFT during freeze-thaw-evaporative cycles. Six columns were constructed, filled with CFT, and put through three consecutive freeze-thaw-evaporative cycles in a controlled environment chamber. Columns were sacrificially sampled before each thaw and evaporative period, where samples were collected from the top to the bottom for porewater analysis. Experimental results showed elevated salts (i.e. Na^+, K^+, Cl^-, SO_4) near the top of the columns after the first thaw and evaporative period. The first thaw period also had maximum water loss, leading to consolidation

of the tailings. An additional capillary break between the CFT and the cover material is necessary to capture the salts, as well as appropriate drainage away from the deposits to limit erosion of the cover material.

Both experiments provided important insights into the long-lasting effect of using oil sands tailings in reclamation technologies. Elevated salt concentrations found in FFT and CFT porewater will be an ongoing issue. Water and soil quality is affected by excess salt, leading to limited plant growth and solidification of cover material. With this knowledge, operators in individual oil sands mines can make changes in reclamation plans for closure landscapes. Sustainable reclamation of the mines can be achieved with this and further research, to ensure vegetation growth and the return of wildlife.

5.1. FUTURE WORK

With the increasing interest in treated tailings and the evaluation of different flocculants and coagulants, there is a need to conduct more research to determine any long-term impacts for FFT reclamation technologies. These additives should be tested at differing amendment rates, individually and combined. Analysis of microbial response to amendments, combined with the headspace gas analysis, can aid in the identification of the microbial presence in the FFT. FFT samples from various locations should be used, to ensure a more complete understanding of the impact.

Further research on CFT geochemistry should examine the salt distribution in CFT during freeze-thaw-evaporative cycles with additional layers – a capillary layer, and cover material – and their impact on salt distribution. The capillary layer should be a higher permeable material to limit interaction between the CFT and the cover material, such as sand or petroleum coke. Testing of

the layers can include the use of saline-tolerant plants to test the sustainable growing ability of the cover material.

REFERENCES

Abolfazlzadehdoshanbehbazari, M., Birks, S.J., Moncur, M.C., Ulrich, A.C. (2013). Fate and transport of oil sand process-affected water into the underlying clay till: A field study. *Journal of Contaminant Hydrology*, 151: 83–92. doi:10.1016/j.jconhyd.2013.05.002

AER (2016). Directive 082: Operating Criteria: Resource Recovery Requirements for Oil Sands Mine and Processing Plant Operations. Calgary: Alberta Energy Regulator.

AER (2017). Directive 085: Fluid Tailings Management for Oil Sands Mining Projects. Calgary: Alberta Energy Regulator.

AER (2019). Water Use Performance: Oil Sands Mining. Calgary: Alberta Energy Regulator.

AER (2020). State of Fluid Tailings Management for Mineable Oil Sands, 2019. Calgary: Alberta Energy Regulator.

Allen, E.W. (2008). Process water treatment in Canada's oil sands industry: I. Target pollutants and treatment objectives. Journal of Environmental Engineering and Science, 7 (2): 123–138. doi:10.1139/S07-038

Alvarez, J., and S. Han. (2013). Current Overview of Cyclic Steam Injection Process. *Journal of Petroleum Science Research*, 2 (3): 116–127.

Banerjee, D.K. (2012). Oil Sands, Heavy Oil & Bitumen: From Recovery to Refinery. Tulsa: PennWell Corporation.

Barton, C.D., and A.D. Karathanasis. (2002). Clay Minerals. In *Encyclopedia of Soil Science*. New York, New York: Marcel Dekker.

Benson, B.B., and D. Krause Jr. (1976). Empirical laws for dilute aqueous solutions of nonpolar gases. *The Journal of Chemical Physics*, 64: 689–709. doi:10.1063/1.443074

Barber, S.A. (1984). Soil Nutrient Bioavailability: A Mechanistic Approach. United States of America: John Wiley & Sons.

Bergerson, J.A., O. Kofoworola, A.D. Charpentier, S. Sleep, and H.L. MacLean. (2012). Life Cycle Greenhouse Gas Emissions of Current Oil Sands Technologies: Surface Mining and In Situ Applications. *Environmental Science & Technology*, 46: 7865–7874. doi:10.1021/es300718h

Bethke, C.M., D. Ding, Q. Jin, and R.A. Sanford. (2008). Origin of microbiological zoning in groundwater flows. *Geology*, 36 (**9**): 739–742. doi:10.1130/G24859A.1

BGC Engineering. (2010). Oil Sands Tailings Technology Review. Edmonton: Oil Sands Research and Information Network, University of Alberta, School of Energy and the Environment.

Bleam, W.F. (2017). Soil and Environmental Chemistry. United States of America: Academic Press.

Brown, D., E. Ramos-Padrón, L. Gieg, G. Voordouw. (2013). Effect of calcium ions and anaerobic microbial activity on sedimentation of oil sands tailings. *International Biodeterioration & Biodegradation*, 81: 9–16. doi:10.1016/j.ibiod.2012.07.006

Bolea, I., A.A. Checa, and L.M. Romeo. (2014). Assessment of the integration of CO2 capture technology into oil– sand extraction operations. *International Journal of Energy and Environmental Engineering*, 5: 323–332. doi:10.1007/s40095-014-0130-4

Booterbaugh, A., L. Bentley, and C. Mendoza. (2015). Geophysical Characterization of an Undrained Dyke Containing an Oil Sands Tailings Pond, Alberta, Canada. *Journal of Environmental & Engineering Geophysics*, 20: 303–317. doi:10.2113/JEEG20.4.303

Carey, S.K. (2008). Growing season energy and water exchange from an oil sands overburden reclamation soil cover, Fort McMurray, Alberta, Canada. *Hydrological Processes*, 22 (**15**): 2847–2857. doi:10.1002/hyp.7026

Chen, M., Gillian W., E. Chi Fru, J.J.H. Ciborowski, and C.G. Weisener. (2013). Microcosm assessment of the biogeochemical development of sulfur and oxygen in oil sands fluid fine tailings. *Applied Geochemistry*, 37: 1–11. doi:10.1016/j.apgeochem.2013.06.007

Cilia, C. (2017). Characterizing the physical and chemical transport of dissolved salts in layered oil sands mine wastes undergoing reclamation [*masters dissertation*]. Retrieved from https://ecommons.usask.ca.

Clark, K.A. (1944). Hot-Water Separation of Alberta Bituminous Sand. *Transactions of the Institution of Mining and Metallurgy*, 47: 257–274. doi:10.1021/ie50276a016

Conly, F.M., R.W. Crosley, and J.V. Headley. (2002). Characterizing sediment sources and natural hydrocarbon inputs in the lower Athabasca River. *Journal of Environmental Engineering and Science*, 1: 187–199. doi:10.1139/s02-013

COSIA (Canada's Oil Sands Innovation Alliance). (2012). Technical Guide for Fluid Fine Tailings Management. [WWW Document]. URL https://www.cosia.ca/sites/default/files/attachments/TechGuideFluidTailingsMgmt_Aug2012.pdf.

Daie, Q., and K.H. Chung. (1996). Hot water extraction process mechanism using model oil sands. *Fuel*, 75 (**2**): 220–226. doi:10.1016/0016-2361(95)00218-9

Das, N., and P. Chandran. (2011). Microbial Degradation of Petroleum Hydrocarbon Contaminants: An Overview. *Biotechnology Research International*, 2011: 1–13. doi:10.4061/2011/941810

Dompierre, K.A., M.B.J. Lindsay, P. Cruz-Hernández, and G. M. Halferdahl. (2016). Initial geochemical characteristics of fluid fine tailings in an oil sands end pit lake. *Science of the Total Environment*, 556: 196–206. doi:10.1002/2016WR020112

Dompierre, K., and S.L. Barbour. (2017). Thermal properties of oil sands fluid fine tailings: laboratory and in situ testing methods. *Canadian Geotechnical Journal*, 54 (**3**): 428–440. doi:10.1139/cgj-2016-0235

Dompierre, K.A., S.L. Barbour, R.L. North, S.K. Carey, and M.B. J. Lindsay. (2017). Chemical mass transport between fluid fine tailings and the overlying water cover of an oil sands end pit lake. *Water Resources Research*, 53 (**6**): 4725–4740. doi:10.1002/2016WR020112

Fedorak, P.M., D.L. Coy, M.J. Dudas, M.J. Simpson, A.J. Renneberg, and M.D. MacKinnon. (2003). Microbially-mediated fugitive gas production from oil sands tailings and increased tailings densification rates. *Journal of Environmental Engineering and Science*, 2: 199–211. doi:10.1139/s03-022

Foght, J.M., L.M. Gieg, and T.Siddique. (2017). The microbiology of oil sands tailings: past, present, future. *FEMS Microbiology Ecology*, 93 (**5**): 1–22. doi:10.1093/femsec/fix034

Francis, D. (2020). Examining Controls on Chemical Mass Transport across the Tailings-Water Interface of an Oil Sands End Pit Lake [*masters dissertation*]. Retrieved from https://ecommons.usask.ca.

Gibson, J.J., J. Fennell, S.J. Birks, Y. Yi, M.C. Moncur, B. Hansen, and S. Jasechko. (2013). Evidence of discharging saline formation water to the Athabasca River in the oil sands mining region, northern Alberta. *Canadian Journal of Earth Sciences*, 50 (12): 1244–1257. doi:10.1139/cjes-2013-0027

Government of Alberta. (2015). Lower Athabasca Region: Tailings Management Framework for the Mineable Athabasca Oil Sands.

Gray, M.R. (2015). Upgrading Oilsands Bitumen and Heavy Oil. Edmonton, Alberta: The University of Alberta Press.

Hach Company. (2018). Alkalinity, Phenolphthalein and Total Alkalinity, Digital Titrator Method 8203. Hach Company, 1–8.

Hach Company. (2020). Nitrogen, Ammonia - Salicylate HR 831/832 Method 10205. Hach Company, 1–4.

Hach Company. (2018). Sulfide - USEPA Methylene Blue Method 8131. Hach Company, 1–6.

Heaton, K. (2015). Biogeochemical Investigation of Centrifuged Fine Tailings Deposits at an Oil Sands Mine in Northern Alberta, Canada [*masters dissertation*]. Retrieved from https://ecommons.usask.ca.

Hein, F.J., and D.K. Cotterill. (2006). The Athabasca Oil Sands – A Regional Geological Perspective, Fort McMurray Area, Alberta, Canada. *Natural Resources Research,* 12 (**2**): 85–102. doi:10.1007/s11053-006-9015-4

Henry, L. (2010). Henry's Handbook of Soil and Water. Saskatoon, Saskatchewan: Henry Perspectives.

Holden, A.A., R.B. Donahue, and A.C. Ulrich. (2011). Geochemical interactions between process-affected water from oil sands tailings ponds and Northern Alberta surficial sediments. *Journal of Contaminant Hydrology*, 119: 55–68. doi:10.1016/j.jconhyd.2010.09.008

Holowenko, F.M., M.D. MacKinnon, and P.M. Fedorak. (2000). Methanogens and sulfate-reducing bacteria in oil sands fine tailings waste. *Canadian Journal of Microbiology*, 46: 927–937. doi:10.1139/w00-081

Hooshiar, A., P. Uhlik, D.G. Ivey, Q. Liu, and T.H. Etsell. (2012). Clay minerals in nonaqueous extraction of bitumen from Alberta oil sands: Part 2. Characterization of clay minerals. *Fuel Processing Technology*, 96: 183–194. doi:10.1016/j.fuproc.2011.10.008

Israelachvili, J.N. (2011). 4 - Interactions Involving Polar Molecules. In *Intermolecular and Surface Forces* (3rd ed.). United States of America: Academic Press.

Jones, K.L., M.B.J. Lindsay, R. Kipfer, K. Ulrich Mayer. (2014). Atmospheric noble gases as tracers of biogenic gas dynamics in a shallow unconfined aquifer. *Geochimica et Cosmochimica Acta,* 128: 144–157. doi:10.1016/j.gca.2013.12.008

Kabwe, L.K., J.D. Scott, N.A. Beier, G.W. Wilson, and S. Jeeravipoolvarn. (2019). Environmental implications of end pit lakes at oil sand mines in Alberta, Canada. *Environmental Geotechnics,* 6(2): 67–74. doi:10.1680/jenge.17.00110

Kasperski, K.L., and R.J. Mikula. (2011). Waste Streams of Mined Oil Sands: Characteristics and Remediation. *Elements,* 7: 387–392. doi:10.2113/gselements.7.6.387

Konhauser, K. (2007). Introduction to Geomicrobiology. Malden, MA: Blackwell Science Ltd.

Kong, J.D., H. Wang, T. Siddique, J. Foght, K. Semple, Z. Burkus, and M.A. Lewis. (2019). Second-generation stoichiometric mathematical model to predict methane emissions from oil sands tailings. *Science of The Total Environment*, 164: 1–9. doi:10.1016/j.scitotenv.2019.133645

Langmuir, D. (1997). Aqueous Environmental Geochemistry. United States of America: Prentice Hall.

Li, X., S.X. Chang, and K. Francis Salifu. (2014). Soil texture and layering effects on water and salt dynamics in the presence of a water table: a review. *Environmental Reviews*, 22 (**1**): 41-50. doi:10.1139/er-2013-0035

Lindsay, M.B.J., C.J. Vessey, and J.M. Robertson. (2019). Mineralogy and geochemistry of oil sands froth treatment tailings: Implications for acid generation and metal(loid) release. *Applied Geochemistry*, 102: 186–196. doi:10.1016/j.apgeochem.2019.02.001

Liu, J., Z. Xu, and J. Masliyah. (2005). Processability of Oil Sand Ores in Alberta. *Energy Fuels*, 19 (**5**): 2056–2063. doi:10.1021/ef050091r

Lo, C.C., B.G. Brownlee, and N.J. Buncea. (2006). Mass spectrometric and toxicological assays of Athabasca oil sands naphthenic acids. *Water Research*, 40: 655– 664. doi:10.1016/j.watres.2005.12.008

Markelova, E., C.T. Parsons, R.-M. Couture, C.M. Smeaton, B. Madé, L. Charlet, and P. Van Cappellen. (2017). Deconstructing the redox cascade: what role do microbial exudates (flavins) play? *Environmental Chemistry*, 14:515–524. doi:10.1071/EN17158

Masliyah, J., Z.J. Zhou, Z. Xu, J. Czarnecki, and H. Hamza. (2004). Understanding Water-Based Bitumen Extraction from Athabasca Oil Sands. *The Canadian Journal of Chemical Engineering*, 82 (4): 628–54. doi:10.1002/cjce.5450820403

Mikula, R. (2012). Advances in oil sands tailings handling: Building the base for reclamation. In *Restoration and Reclamation of Boreal Ecosystems: Attaining Sustainable Development*. Cambridge: Cambridge University Press.

Natural Resources Canada. (2016). Oil Sands Extraction and Processing. [WWW Document]. URL https://www.nrcan.gc.ca/energy/energy-sources-distribution/crude-oil/oil-sands-extraction-and-processing/18094.

Ong, S.K. (2007). Wastewater Engineering. In *Handbook of Environmental Engineering*. United States of America: John Wiley & Sons.

Osacky, M., M. Geramian, Q. Liu, D.G. Ivey, and T.H. Etsell. (2014). Surface properties of petrologic end-members from Alberta oil sands and their relationship with mineralogical and chemical composition. *Energy Fuels*, 28 (**2**): 934–944. doi:10.1021/ef402150z

Ramos-Padrón, E., S. Bordenave, S. Lin, I. Mani Bhaskar, X. Dong, C.W. Sensen, J. Fournier, G. Voordouw, and L.M. Gieg. (2011). Carbon and Sulfur Cycling by Microbial Communities in a Gypsum-Treated Oil Sands Tailings Pond. *Environmental Science & Technology*, 45 (**2**): 439–446. doi:10.1021/es1028487

Rima, U.S., and S. Azam. (2015). Centrifuge dewatering of polymer-amended oil sands tailings. *Environmental Geotechnics*, 2 (**EG3**): 175–180. doi:10.1680/envgeo.13.00083

Rudderham, S. (2019). Geomicrobiology and Geochemistry of Fluid Fine Tailings in an Oil Sands End Pit Lake [*masters dissertation*]. Retrieved from https://ecommons.usask.ca.

Siddique, T., P. Kuznetsov, A. Kuznetsova, N. Arkell, R. Young, C. Li, S. Guigard, E. Underwood, and J.M. Foght. (2014). Microbially-accelerated consolidation of oil sands tailings. Pathway I: changes in porewater chemistry. *Frontiers in Microbiology*, 5 (**106**): 1–11. doi:10.3389/fmicb.2014.00107

Siddique, T., T. Penner,J. Klassen, C. Nesbø, and J.M. Foght. (2012). Microbial Communities Involved in Methane Production from Hydrocarbons in Oil Sands Tailings. *Environmental Science & Technology*, 46: 9802−9810. doi: 10.1021/es302202c.

Simhayov, R.B., J.S. Price, C.M. Smeaton, C. Parsons, F. Rezanezhad, and P. Van Cappellen. (2017). Solute pools in Nikanotee Fen watershed in the Athabasca oil sands region. *Environmental Pollution*, 225: 150-162. doi:10.1016/j.envpol.2017.03.038

Shainberg, I., and G.J. Levy. (2005). Flocculation and Dispersion. In *Encyclopedia of Soils in the Environment* (3rd ed.). United States of America: Elsevier Ltd.

Small, C.C., S. Cho, S. Hashisho, and A.C. Ulrich. (2015). Emissions from oil sands tailings ponds: Review of tailings pond parameters and emission estimates. *Journal of Petroleum Science and Engineering*, 127: 490–501. doi:10.1016/j.petrol.2014.11.020

Sollins, P., G.P. Robertson, and G. Uehara. (1988). Nutrient mobility in variable- and permanent-charge soils. *Biogeochemistry*, 6 (3): 181–199. doi:10.1007/BF02182995

Sposito, G., N.T. Skipper, R. Sutton, Sung-ho Park, A.K. Soper, and J.A. Greathouse. (1999). Surface geochemistry of the clay minerals. *Proceedings of the National Academy of Sciences of the United States of America*, 96: 3358–3364. doi:10.1073/pnas.96.7.3358

Stasik, S., N. Loic, K. Knölle, C. Weisener, and K. Wendt-Potthoff. (2014). Understanding biogeochemical gradients of sulfur, iron and carbon in an oil sands tailings pond. *Chemical Geology*, 382: 44–53. doi:10.1016/j.chemgeo.2014.05.026

Stasik, S., and K. Wendt-Potthoff. (2016). Vertical gradients in carbon flow and methane production in a sulfate-rich oil sands tailings pond. *Water Research*, 106: 223–231. doi:10.1016/j.watres.2016.09.053

Syncrude. (2017). Understanding Our Process. [WWW Document]. URL http://www.syncrude.ca/our-process/understanding-our-process/.

Ugochukwu, U.C. (2019). Characteristics of clay minerals relevant to bioremediation of environmental contaminated systems. In *Modified Clay and Zeolite Nanocomposite Materials: Environmental and Pharmaceutical Applications*. Amsterdam, Netherlands: Elsevier.

Vessey, C.J., M.B.J. Lindsay, and S.L. Barbour. (2019). Sodium transport and attenuation in soil cover materials for oil sands mine reclamation. *Applied Geochemistry*, 100: 42–54. doi:10.1016/j.apgeochem.2018.10.023

Wilhelm, E., R. Battino, and R.J. Wilcock. (1977). Low-pressure solubility of gases in liquid water. *Chemical Reviews*, 77 (**2**): 219–262. doi:10.1021/ cr60306a003

APPENDIX A: BATCH EXPERIMENTAL DATA

Table A-1: Carbon dioxide (CO_2) for the batch experiment, with one standard deviation.

Week	MC-0.00 (mg L^{-1})	MC-0.25 (mg L^{-1})	MC-0.50 (mg L^{-1})	MC-1.00 (mg L^{-1})	MC-2.00 (mg L^{-1})
0	8.33 ± 9.73	4.82 ± 3.58	7.61 ± 7.17	6.53 ± 5.07	6.74 ± 4.98
2	51.95 ± 38.75	51.78 ± 38.21	46.19 ± 53.34	73.07 ± 53.15	105.72 ± 86.08
4	43.18 ± 31.53	23.08 ± 30.49	61.90 ± 48.09	72.13 ± 53.37	75.39 ± 92.75
8	48.59 ± 35.14	63.73 ± 47.53	68.66 ± 50.94	76.70 ± 56.99	110.78 ± 83.97
16	53.50 ± 42.24	61.50 ± 47.34	56.00 ± 39.82	71.15 ± 55.74	103.08 ± 79.28
32	56.45 ± 43.45	57.97 ± 49.15	70.68 ± 51.64	103.34 ± 85.39	98.36 ± 76.46
64	64.26 ± 47.46	80.24 ± 62.33	80.47 ± 59.78	93.43 ± 73.15	129.29 ± 97.23

Table A-2: Methane (CH_4) for the batch experiment, with one standard deviation.

Week	MC-0.00 (mg L^{-1})	MC-0.25 (mg L^{-1})	MC-0.50 (mg L^{-1})	MC-1.00 (mg L^{-1})	MC-2.00 (mg L^{-1})
0	0.86 ± 1.10	0.62 ± 0.25	0.95 ± 0.55	1.64 ± 0.41	1.10 ± 0.61
2	5.81 ± 1.80	7.35 ± 4.44	13.47 ± 3.49	11.83 ± 5.93	13.21 ± 7.11
4	12.75 ± 7.21	14.15 ± 7.70	15.16 ± 2.78	15.08 ± 4.11	18.54 ± 4.54
8	15.95 ± 7.65	23.86 ± 3.12	25.05 ± 4.65	21.43 ± 4.78	23.89 ± 7.19
16	18.75 ± 8.76	22.36 ± 8.31	22.44 ± 10.59	23.27 ± 12.04	24.56 ± 9.55
32	20.26 ± 12.87	18.97 ± 8.23	22.59 ± 8.18	22.13 ± 7.90	16.31 ± 10.36
64	16.10 ± 8.41	22.72 ± 9.16	22.48 ± 9.54	17.86 ± 10.18	24.01 ± 11.31

Table A-3: pH for the batch experiment, with one standard deviation.

Week	MC-0.00	MC-0.25	MC-0.50	MC-1.00	MC-2.00
0	8.12 ± 0.07	8.11 ± 0.04	8.07 ± 0.07	8.03 ± 0.02	7.86 ± 0.06
2	8.05 ± 0.05	8.04 ± 0.09	7.92 ± 0.04	7.90 ± 0.19	7.68 ± 0.10
4	8.01 ± 0.05	7.95 ± 0.07	7.93 ± 0.06	7.77 ± 0.05	7.69 ± 0.13
8	8.00 ± 0.04	7.91 ± 0.05	7.84 ± 0.03	7.70 ± 0.03	7.62 ± 0.08
16	8.00 ± 0.06	7.93 ± 0.04	7.83 ± 0.04	7.77 ± 0.05	7.58 ± 0.03
32	8.09 ± 0.13	8.04 ± 0.15	7.96 ± 0.11	7.79 ± 0.24	7.68 ± 0.17
64	7.92 ± 0.04	7.87 ± 0.03	7.79 ± 0.04	7.69 ± 0.05	7.56 ± 0.05

Table A-4: Reduction Potential (Eh) for the batch experiment, with one standard deviation.

Week	MC-0.00	MC-0.25	MC-0.50	MC-1.00	MC-2.00
	mV	mV	mV	mV	mV
0	299.53 ± 37.99	322.81 ± 45.23	306.40 ± 40.39	313.36 ± 35.66	322.07 ± 33.04
2	326.93 ± 10.62	316.61 ± 16.22	323.92 ± 9.24	267.57 ± 26.20	317.88 ± 29.38
4	269.25 ± 13.77	306.64 ± 21.06	307.10 ± 20.95	297.37 ± 8.70	305.26 ± 3.26
8	430.09 ± 22.21	389.90 ± 23.59	384.63 ± 26.92	349.73 ± 6.31	355.40 ± 32.31
16	383.46 ± 56.30	347.96 ± 56.57	328.29 ± 42.92	328.38 ± 32.58	331.36 ± 26.33
32	310.42 ± 44.82	308.74 ± 37.44	307.85 ± 19.62	330.78 ± 13.07	315.05 ± 19.42
64	235.44 ± 53.62	238.14 ± 14.11	210.37 ± 52.63	238.00 ± 39.26	287.01 ± 72.09

Table A-4: Alkalinity for the batch experiment, with one standard deviation.

Week	MC-0.00 (mg L^{-1} as $CaCO_3$)	MC-0.25 (mg L^{-1} as $CaCO_3$)	MC-0.50 (mg L^{-1} as $CaCO_3$)	MC-1.00 (mg L^{-1} as $CaCO_3$)	MC-2.00 (mg L^{-1} as $CaCO_3$)
0	1067.41 ± 129.05	1099.92 ± 32.86	1005.35 ± 133.17	947.33 ± 76.43	1040.65 ± 59.02
2	952.19 ± 53.35	999.32 ± 18.99	1006.04 ± 32.77	893.42 ± 62.88	847.19 ± 40.33
4	1014.06 ± 59.01	907.35 ± 179.91	873.97 ± 117.90	699.61 ± 159.18	793.81 ± 80.18
8	1050.49 ± 69.04	925.35 ± 38.81	837.81 ± 123.63	772.96 ± 137.25	794.02 ± 100.42
16	984.05 ± 50.37	965.93 ± 121.00	932.18 ± 121.43	838.92 ± 53.83	825.05 ± 50.86
32	1054.00 ± 128.11	979.27 ± 102.67	985.35 ± 70.01	699.10 ± 206.30	799.22 ± 29.39
64	1253.31 ± 82.66	1173.13 ± 106.69	1132.48 ± 67.89	977.37 ± 52.05	892.77 ± 76.31

Table A-5: Calcium (Ca) for the batch experiment, with one standard deviation.

Week	MC-0.00 (mg L^{-1})	MC-0.25 (mg L^{-1})	MC-0.50 (mg L^{-1})	MC-1.00 (mg L^{-1})	MC-2.00 (mg L^{-1})
0	19.24 ± 1.31	32.12 ± 10.83	35.69 ± 1.28	43.42 ± 18.92	111.27 ± 11.62
2	19.34 ± 0.99	26.97 ± 1.53	35.59 ± 0.19	61.65 ± 0.51	146.88 ± 2.53
4	18.88 ± 0.85	25.95 ± 0.44	34.20 ± 1.67	60.32 ± 2.01	147.78 ± 1.05
8	18.76 ± 0.27	25.84 ± 0.71	34.73 ± 1.18	60.09 ± 1.82	145.51 ± 1.84
16	19.67 ± 1.24	25.73 ± 1.72	35.64 ± 0.93	61.21 ± 1.03	148.73 ± 1.57
32	17.89 ± 1.79	25.34 ± 1.57	34.09 ± 1.27	58.67 ± 1.67	141.94 ± 2.82
64	17.01 ± 1.04	24.01 ± 1.87	32.47 ± 0.81	57.48 ± 1.62	139.26 ± 1.20

Table A-6: Sodium (Na) for the batch experiment, with one standard deviation.

Week	MC-0.00 ($mg\ L^{-1}$)	MC-0.25 ($mg\ L^{-1}$)	MC-0.50 ($mg\ L^{-1}$)	MC-1.00 ($mg\ L^{-1}$)	MC-2.00 ($mg\ L^{-1}$)
0	823.80 ± 26.13	879.70 ± 41.65	893.47 ± 9.83	910.24 ± 67.85	1050.25 ± 33.72
2	825.76 ± 9.24	876.56 ± 21.22	905.82 ± 6.89	1034.15 ± 87.36	1073.50 ± 7.21
4	830.94 ± 8.45	867.11 ± 0.88	903.86 ± 3.19	971.42 ± 7.45	1073.55 ± 14.78
8	821.54 ± 8.27	864.25 ± 6.51	892.62 ± 9.42	978.60 ± 14.84	1082.53 ± 4.07
16	860.34 ± 6.66	875.92 ± 9.06	928.08 ± 5.42	991.43 ± 10.26	1106.74 ± 5.32
32	864.01 ± 26.40	903.43 ± 24.18	949.08 ± 25.47	1033.15 ± 40.09	1136.39 ± 51.14
64	862.28 ± 21.09	898.06 ± 12.35	934.51 ± 11.65	1039.92 ± 49.13	1111.19 ± 26.25

Table A-7: Magnesium (Mg) for the batch experiment, with one standard deviation.

Week	MC-0.00 ($mg\ L^{-1}$)	MC-0.25 ($mg\ L^{-1}$)	MC-0.50 ($mg\ L^{-1}$)	MC-1.00 ($mg\ L^{-1}$)	MC-2.00 ($mg\ L^{-1}$)
0	9.93 ± 0.64	13.83 ± 2.92	15.17 ± 0.79	16.93 ± 5.44	31.35 ± 2.39
2	10.18 ± 0.15	12.89 ± 0.47	15.73 ± 0.21	22.64 ± 0.18	38.20 ± 0.49
4	9.98 ± 0.32	12.53 ± 0.20	15.07 ± 0.35	21.93 ± 0.68	37.43 ± 0.58
8	10.01 ± 0.43	12.52 ± 0.50	15.17 ± 0.14	21.91 ± 0.36	37.91 ± 0.84
16	10.47 ± 0.45	12.47 ± 0.58	15.66 ± 0.36	22.46 ± 0.35	39.94 ± 0.18
32	9.93 ± 0.80	12.72 ± 0.68	15.28 ± 0.42	21.91 ± 0.47	39.32 ± 1.49
64	9.55 ± 0.48	12.17 ± 0.81	14.82 ± 0.21	23.84 ± 6.52	39.07 ± 0.78

Table A-8: Potassium (K) for the batch experiment, with one standard deviation.

Week	MC-0.00 ($mg\ L^{-1}$)	MC-0.25 ($mg\ L^{-1}$)	MC-0.50 ($mg\ L^{-1}$)	MC-1.00 ($mg\ L^{-1}$)	MC-2.00 ($mg\ L^{-1}$)
0	24.58 ± 7.02	62.82 ± 64.28	23.86 ± 0.82	26.74 ± 4.56	35.58 ± 12.22
2	36.81 ± 9.13	18.3 ± 0.45	20.13 ± 0.78	25.11 ± 0.48	28.71 ± 1.40
4	30.07 ± 5.80	43.11 ± 29.28	20.19 ± 0.33	23.54 ± 1.64	31.72 ± 7.71
8	208.48 ± 145.37	82.86 ± 40.81	61.77 ± 6.84	99.77 ± 34.38	58.62 ± 28.60
16	164.79 ± 78.89	51.99 ± 18.09	68.37 ± 27.68	37.85 ± 5.22	40.81 ± 17.94
32	124.37 ± 45.66	48.44 ± 15.59	52.33 ± 25.71	56.97 ± 23.13	74.01 ± 15.46
64	64.91 ± 33.62	49.13 ± 14.52	52.02 ± 11.67	39.46 ± 10.71	58.37 ± 11.51

Table A-9: Hydrogen sulfide (ΣH_2S) for the batch experiment, with one standard deviation.

Week	MC-0.00 ($\mu g\ L^{-1}$)	MC-0.25 ($\mu g\ L^{-1}$)	MC-0.50 ($\mu g\ L^{-1}$)	MC-1.00 ($\mu g\ L^{-1}$)	MC-2.00 ($\mu g\ L^{-1}$)
0	53.86 ± 36.31	77.02 ± 17.57	86.05 ± 49.10	33.50 ± 9.45	30.12 ± 11.08
2	58.23 ± 18.57	63.78 ± 15.93	66.28 ± 11.54	35.86 ± 17.08	40.63 ± 29.52
4	70.75 ± 32.41	74.75 ± 33.12	57.25 ± 10.48	43.25 ± 19.00	26.75 ± 11.98
8	72.04 ± 23.07	84.93 ± 28.40	60.21 ± 10.72	58.79 ± 18.39	29.96 ± 6.14
16	109.86 ± 51.02	92.29 ± 23.79	71.32 ± 26.85	53.43 ± 21.32	33.53 ± 16.65
32	109.20 ± 45.26	98.74 ± 19.39	72.47 ± 28.59	42.86 ± 24.36	45.68 ± 40.31
64	235.13 ± 60.88	199.38 ± 84.58	202.81 ± 15.82	218.75 ± 56.51	140.63 ± 35.59

Table A-10: Sulfate (SO_4) for the batch experiment, with one standard deviation.

Week	MC-0.00 (mg L^{-1})	MC-0.25 (mg L^{-1})	MC-0.50 (mg L^{-1})	MC-1.00 (mg L^{-1})	MC-2.00 (mg L^{-1})
0	100.10 ± 36.44	208.00 ± 39.23	384.00 ± 20.30	604.00 ± 97.78	1040.00 ± 30.00
2	141.25 ± 14.57	298.00 ± 20.42	442.00 ± 22.11	802.00 ± 25.27	1430.00 ± 36.74
4	125.67 ± 46.92	280.86 ± 45.15	445.69 ± 23.43	768.94 ± 12.06	1432.32 ± 20.58
8	117.78 ± 34.45	248.80 ± 29.15	372.38 ± 10.17	726.60 ± 38.12	1437.78 ± 12.56
16	77.52 ± 39.62	239.01 ± 41.23	361.70 ± 32.68	713.98 ± 48.48	1417.37 ± 18.63
32	107.87	210.26 ± 19.87	350.13 ± 19.92	694.58 ± 1096.49	1404.93 ± 461.74
64	44.87 ± 14.05	211.07 ± 19.89	377.55 ± 20.91	653.81 ± 17.17	1343.26 ± 17.66

Table A-11: Sulfur (S) for the batch experiment, with one standard deviation.

Week	MC-0.00 (mg L^{-1})	MC-0.25 (mg L^{-1})	MC-0.50 (mg L^{-1})	MC-1.00 (mg L^{-1})	MC-2.00 (mg L^{-1})
0	35.80 ± 13.50	111.24 ± 52.51	130.19 ± 5.09	160.27 ± 87.82	351.24 ± 13.28
2	51.48 ± 6.35	102.97 ± 4.13	149.24 ± 5.73	264.59 ± 13.34	482.03 ± 13.84
4	45.50 ± 16.83	98.83 ± 15.82	153.10 ± 5.82	262.35 ± 6.31	483.35 ± 10.54
8	46.21 ± 15.04	91.29 ± 9.86	146.07 ± 3.86	251.68 ± 11.17	474.52 ± 6.27
16	36.82 ± 16.34	95.66 ± 13.70	149.59 ± 8.76	267.45 ± 14.18	498.83 ± 12.77
32	30.54 ± 17.77	94.37 ± 7.81	144.57 ± 7.02	269.37 ± 6.30	559.44 ± 28.94
64	25.34 ± 4.85	82.33 ± 8.11	139.04 ± 7.00	262.71 ± 9.55	512.21 ± 9.07

Table A-11: Iron (Fe) for the batch experiment, with one standard deviation.

Week	MC-0.00 (mg L^{-1})	MC-0.25 (mg L^{-1})	MC-0.50 (mg L^{-1})	MC-1.00 (mg L^{-1})	MC-2.00 (mg L^{-1})
0	0.012 ± 0.004	0.012 ± 0.005	0.017 ± 0.005	0.007 ± 0.003	0.016 ± 0.011
2	0.010 ± 0.003	0.008 ± 0.002	0.007 ± 0.002	0.009 ± 0.003	0.302 ± 0.504
4	0.016 ± 0.002	0.012 ± 0.006	0.024 ± 0.020	0.008 ± 0.004	0.013 ± 0.017
8	0.008 ± 0.002	0.008 ± 0.004	0.008 ± 0.005	0.017 ± 0.016	0.140 ± 0.222
16					
32	0.015 ± 0.007	0.010 ± 0.003	0.009 ± 0.003	0.012 ± 0.005	0.296 ± 0.293
64	0.017 ± 0.005	0.017 ± 0.007	0.020 ± 0.011	0.078 ± 0.084	0.252 ± 0.207

APPENDIX B: COLUMN EXPERIMENTAL DATA

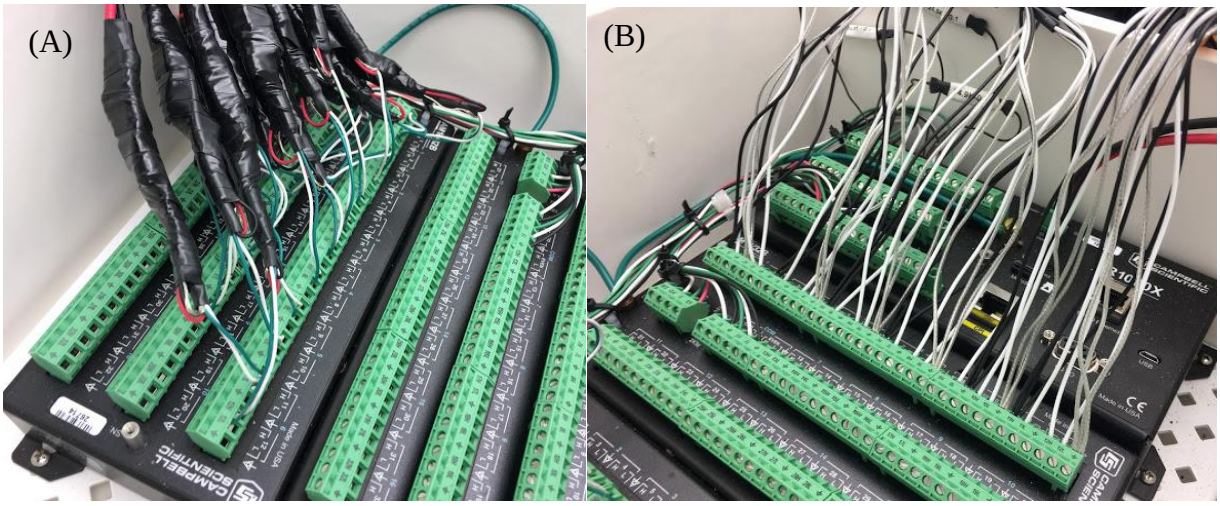

Figure B-1: Load cells (A) and temperature probes (B) connected to the CR1000X data logger for six columns.

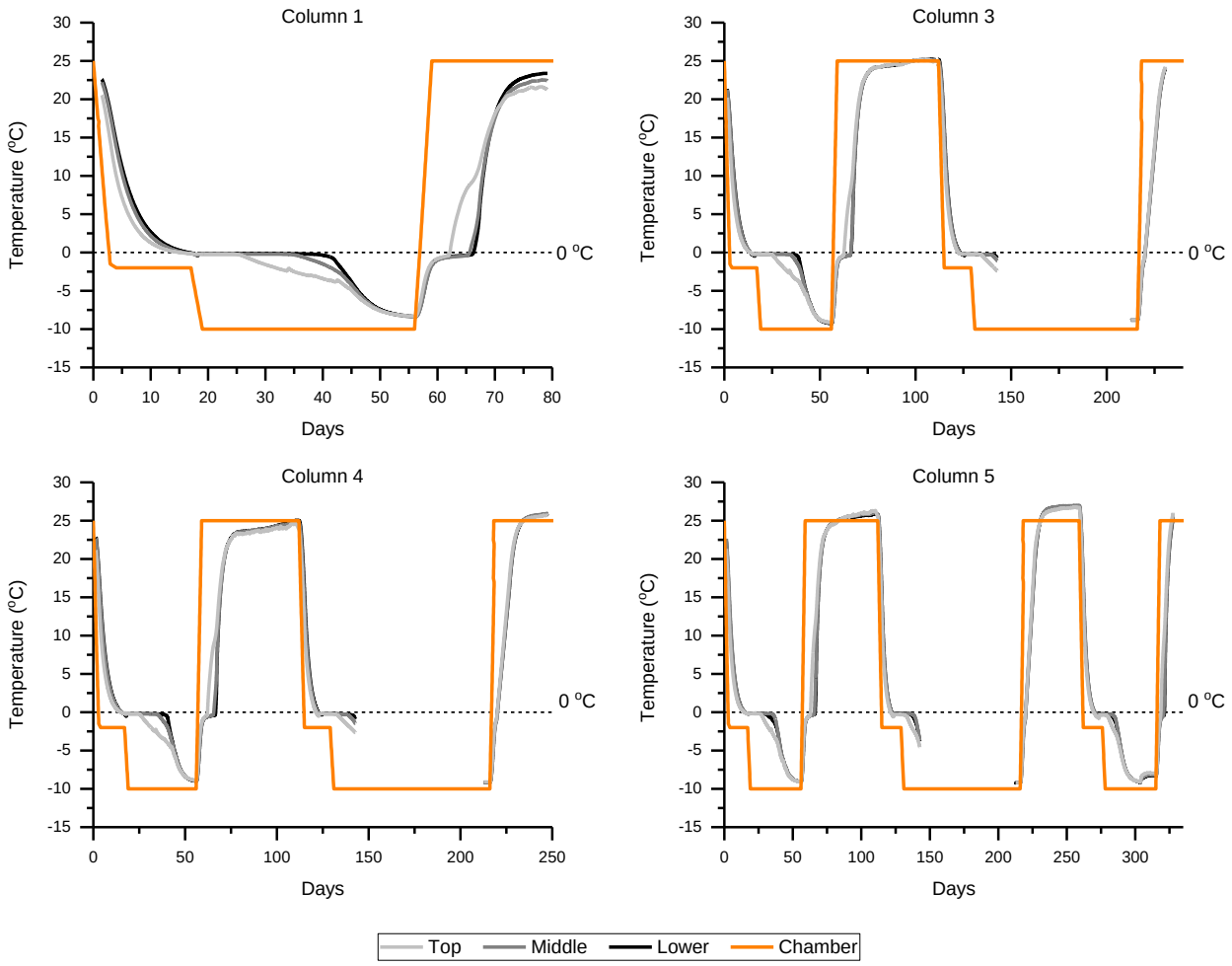

Figure B-2: Temperature probes (upper, middle, and lower) in Columns 1, 3, 4, and 5 over the course of the experiment. Orange line is set temperature in the chamber.

Table B-1: pH for the column experiment. Initial refers to porewater collected during filling of the columns; final refers to porewater collected during that columns deconstructive sampling.

Height	Column 1		Column 2		Column 3		Column 4		Column 5		Column 6	
(cm)	Initial	Final	Initial	Final	Initial	Final	Initial	Final	Initial	Final	Initial	Final
73.5			7.69		7.62						7.70	
63			7.42									
60									7.78			
52.5	7.71		7.77		7.70		7.68		7.61		7.75	
31.5			7.28		7.50		7.60		7.92		7.74	
10.5	7.64		7.56		7.44		7.71		7.67			
48.25-46		7.52		7.48		7.48		7.56		7.54		7.91
30		7.50		6.96		7.31		7.40		6.96		7.27
20		7.47		7.28		6.96		7.47		7.00		6.82
12.5		7.15		7.33		6.59		7.05		6.98		7.01
7.5		7.08		6.59		6.62		7.09				
2.5		7.21		7.07								

Table B-2: Electrical conductivity (EC) for the column experiment. Initial refers to porewater collected during filling of the columns; final refers to porewater collected during that columns deconstructive sampling.

Height	Column 1		Column 2		Column 3		Column 4		Column 5		Column 6	
(cm)	Initial (mS cm^{-1})	Final (mS cm^{-1})	Initial (mS cm^{-1})	Final (mS cm^{-1})	Initial (mS cm^{-1})	Final (mS cm^{-1})	Initial (mS cm^{-1})	Final (mS cm^{-1})	Initial (mS cm^{-1})	Final (mS cm^{-1})	Initial (mS cm^{-1})	Final (mS cm^{-1})
73.5			3.52		3.47						3.22	
63			3.87									
60									3.20			
52.5	3.19		3.55		3.50		3.16		3.63		3.17	
31.5			4.26		4.04		3.55		3.38		3.47	
10.5	3.52		3.63		4.05		3.61		3.24			
48.25-46		5.10		3.33		4.13		4.49		7.42		5.08
30		4.23		8.50		4.70		6.18		7.36		8.11
20		4.69		5.20		6.46		7.63		8.82		7.50
12.5		8.30		5.18		9.34		7.61		5.94		9.08
7.5		8.83		8.00		12.83		15.99				
2.5		13.30		15.97								

Table B-3: Alkalinity for the column experiment. Initial refers to porewater collected during filling of the columns; final refers to porewater collected during that columns deconstructive sampling.

Height	Column 1		Column 2		Column 3		Column 4		Column 5		Column 6	
	Initial	Final	Initial	Final	Initial	Final	Initial	Final	Initial	Final	Initial	Final
(cm)	(mg L^{-1} as $CaCO_3$)		(mg L^{-1} as $CaCO_3$)		(mg L^{-1} as $CaCO_3$)		(mg L^{-1} as $CaCO_3$)		(mg L^{-1} as $CaCO_3$)		(mg L^{-1} as $CaCO_3$)	
73.5			1550.70		1438.52						1254.98	
63			1018.92									
60									1175.30			
52.5	1160.00		1404.37		1428.31		1220.00		1260.00		1095.62	
31.5			849.01		1025.88		1360.00		1297.41		1300.00	
10.5	1458.54		1445.65		1335.97		1460.00		1195.22			
48.25-46		460.92		1040.00		738.52		600.00		185.71		240.00
30		658.68		410.42		820.00		580.00		439.12		80.16
20		578.84		558.88		280.56		319.36		122.40		112.00
12.5		400.00		223.54		220.00		200.00		87.41		114.29
7.5		186.79		250.84		119.21		75.47				
2.5		211.00										

Table B-4: Ammonia for the column experiment. Initial refers to porewater collected during filling of the columns; final refers to porewater collected during that columns deconstructive sampling.

Height	Column 1		Column 2		Column 3		Column 4		Column 5		Column 6	
	Initial	Final	Initial	Final	Initial	Final	Initial	Final	Initial	Final	Initial	Final
(cm)	(mg L^{-1})		(mg L^{-1})		(mg L^{-1})		(mg L^{-1})		(mg L^{-1})		(mg L^{-1})	
73.5			17.8		11.8						10.2	
63			20.8									
60									13.0			
52.5	11.7		16.7		17.3		11.5		13.3		11.5	
31.5			24.4		18.5		17.7		11.2		17.9	
10.5	18.4		19.7		10.3		15.6		11.1			
48.25-46		0.0		9.1		20.3		19.1		22.2		17.4
30		7.3		12.5		16.1		21.4		2.3		2.3
20		9.4		9.4		1.2		10.9				
12.5		14.1		10.0								
7.5		18.4		0.1								
2.5		12.7		4.4								

Table B-5: Calcium (Ca) for the column experiment. Initial refers to porewater collected during filling of the columns; final refers to porewater collected during that columns deconstructive sampling.

Height	Column 1		Column 2		Column 3		Column 4		Column 5		Column 6	
	Initial	Final	Initial	Final	Initial	Final	Initial	Final	Initial	Final	Initial	Final
(cm)	(mg L^{-1})		(mg L^{-1})		(mg L^{-1})		(mg L^{-1})		(mg L^{-1})		(mg L^{-1})	
73.5			39.61		41.65						21.03	
63			54.67									
60									29.76			
52.5	24.12		42.28		37.81		20.77		45.50		19.70	
31.5			100.32		67.75		41.32		40.70		36.94	
10.5	38.89		42.12		38.67		46.15		20.94			
48.25-46		143.06		40.13		63.45		92.98		416.84		155.13
30		59.05		646.91		122.99		179.37		486.39		612.69
20		76.55		194.83		424.07		437.73		443.76		510.41
12.5		537.15		194.60		375.80		473.50				521.60
7.5		554.45		445.33		375.31						
2.5		553.34		428.99								

Table B-6: Sodium (Na) for the column experiment. Initial refers to porewater collected during filling of the columns; final refers to porewater collected during that columns deconstructive sampling.

Height	Column 1		Column 2		Column 3		Column 4		Column 5		Column 6	
	Initial	Final	Initial	Final	Initial	Final	Initial	Final	Initial	Final	Initial	Final
(cm)	(mg L^{-1})		(mg L^{-1})		(mg L^{-1})		(mg L^{-1})		(mg L^{-1})		(mg L^{-1})	
73.5			777.17		746.71						721.35	
63			787.18									
60									717.36			
52.5	725.21		808.67		762.68		757.18		815.32		704.46	
31.5			850.26		820.07		857.18		738.46		769.18	
10.5	814.71		795.62		758.80		772.23		721.08			
48.25-46		982.33		802.02		960.11		990.79		1317.07		985.80
30		909.47		1559.81		1090.30		1292.99		1226.04		1447.15
20		1019.96		1083.6		1088.71		1437.82		1304.53		1394.09
12.5		1495.06		1136.88		1319.65		1561.25				1549.76
7.5		1614.55		1513.06		2957.22						
2.5		2884.29		5353.12								

Table B-7: Magnesium (Mg) for the column experiment. Initial refers to porewater collected during filling of the columns; final refers to porewater collected during that columns deconstructive sampling.

Height	Column 1		Column 2		Column 3		Column 4		Column 5		Column 6	
	Initial	Final	Initial	Final	Initial	Final	Initial	Final	Initial	Final	Initial	Final
(cm)	(mg L^{-1})		(mg L^{-1})		(mg L^{-1})		(mg L^{-1})		(mg L^{-1})		(mg L^{-1})	
73.5			18.64		27.49						14.43	
63			28.51									
60									17.25			
52.5	14.88		19.31		19.29		13.86		23.07		13.51	
31.5			44.25		32.76		20.11		26.50		19.38	
10.5	18.30		21.12		25.07		30.19		14.63			
48.25-46		85.22		20.65		40.79		62.99		215.13		74.84
30		35.09		251.71		63.81		101.95		293.83		285.44
20		44.80		85.86		253.14		198.86		584.46		249.70
12.5		231.02		87.77		980.35		355.99				504.80
7.5		242.78		347.57		2069.29						
2.5		318.32		574.45								

Table B-8: Potassium (K) for the column experiment. Initial refers to porewater collected during filling of the columns; final refers to porewater collected during that columns deconstructive sampling.

Height	Column 1		Column 2		Column 3		Column 4		Column 5		Column 6	
	Initial	Final	Initial	Final	Initial	Final	Initial	Final	Initial	Final	Initial	Final
(cm)	(mg L^{-1})		(mg L^{-1})		(mg L^{-1})		(mg L^{-1})		(mg L^{-1})		(mg L^{-1})	
73.5			16.60		15.74						13.90	
63			19.17									
60									14.38			
52.5	15.89		16.58		16.51		12.90		17.84		13.61	
31.5			19.71		17.60		15.76		15.01		16.75	
10.5	16.60		17.93		14.48		16.87		14.33			
48.25-46		19.96		15.48		25.13		32.43		72.32		93.70
30		24.36		55.96		32.49		40.93		63.02		103.20
20		46.45		102.27		40.65		52.45		62.72		90.42
12.5		55.98		63.95		64.32		53.10				251.27
7.5		59.04		70.84		179.34						
2.5		81.21		179.72								

Table B-9: Chloride (Cl) for the column experiment. Initial refers to porewater collected during filling of the columns; final refers to porewater collected during that columns deconstructive sampling.

Height	Column 1		Column 2		Column 3		Column 4		Column 5		Column 6	
	Initial	Final	Initial	Final	Initial	Final	Initial	Final	Initial	Final	Initial	Final
(cm)	(mg L^{-1})		(mg L^{-1})		(mg L^{-1})		(mg L^{-1})		(mg L^{-1})		(mg L^{-1})	
73.5			363.70		384.46						395.73	
63			382.54									
60									394.81			
52.5	385.97		364.48		370.67		392.33		373.25		391.33	
31.5			383.58		380.18		370.63		368.98		363.12	
10.5	364.60		363.54		383.79		381.77		397.29			
48.25-46		420		470		460		450		380		495
30		460		400		440		460		320		410
20		450		490		450		470		290		430
12.5		460		470		440		620				800
7.5		470		450		1300		1400				
2.5		1100		2200								

Table B-10: Hydrogen sulfide (ΣH_2S) for the column experiment. Initial refers to porewater collected during filling of the columns; final refers to porewater collected during that columns deconstructive sampling.

Height	Column 1		Column 2		Column 3		Column 4		Column 5		Column 6	
	Initial	Final	Initial	Final	Initial	Final	Initial	Final	Initial	Final	Initial	Final
(cm)	(µg L^{-1})		(µg L^{-1})		(µg L^{-1})		(µg L^{-1})		(µg L^{-1})		(µg L^{-1})	
73.5			4.72		4.72						10.63	
63			17.72									
60									10.63			
52.5	2.36		3.54		5.91		17.72		4.72		3.54	
31.5			2.13				16.54		2.13		10.63	
10.5	9.45		23.62		14.17		25.98		4.72			
48.25-46		0.00		4.25		7.44		1.06		3.19		3.19
30		6.38		5.31		5.31		3.19		10.63		7.44
20		8.50		7.44		7.44		4.25				9.57
12.5		5.31		2.13		3.19		1.06				
7.5		1.06										
2.5		1.06										

Table B-11: Sulfate (SO_4) for the column experiment. Initial refers to porewater collected during filling of the columns; final refers to porewater collected during that columns deconstructive sampling.

Height	Column 1		Column 2		Column 3		Column 4		Column 5		Column 6	
	Initial	Final	Initial	Final	Initial	Final	Initial	Final	Initial	Final	Initial	Final
(cm)	(mg L^{-1})		(mg L^{-1})		(mg L^{-1})		(mg L^{-1})		(mg L^{-1})		(mg L^{-1})	
73.5			51.34		18.77						20.56	
63			628.57									
60									23.60			
52.5	31.81		59.45		58.94		3.79		135.53		14.43	
31.5			891.93		56.36		38.25		22.03		87.56	
10.5	42.65		38.07		565.78		23.80		16.52			
48.25-46		1700		170		1100		1700		4100		1550
30		810		5400		1600		2700		4300		4900
20		1200		2100		3800		4300		6000		4300
12.5		4900		2000		7000		5000				5700
7.5		5100		5400		14000		12000				
2.5		7200		10000								

Table B-12: Iron (Fe) for the column experiment. Initial refers to porewater collected during filling of the columns; final refers to porewater collected during that columns deconstructive sampling.

Height	Column 1		Column 2		Column 3		Column 4		Column 5		Column 6	
	Initial	Final	Initial	Final	Initial	Final	Initial	Final	Initial	Final	Initial	Final
(cm)	(mg L^{-1})		(mg L^{-1})		(mg L^{-1})		(mg L^{-1})		(mg L^{-1})		(mg L^{-1})	
73.5			0.053		0.021						0.040	
63			0.038									
60									0.017			
52.5	0.065		0.016		0.021		0.148		0.028		0.037	
31.5			0.014		0.011		0.028		0.029		0.021	
10.5	0.045		0.036		0.024		0.012		0.068			
48.25-46		0.006		0.063		0.009		0.004		ud		ud
30		0.132		ud		0.009		0.006		ud		ud
20		0.006		0.002		ud		ud		ud		ud
12.5		ud		0.002		ud		ud				ud
7.5		ud		ud		ud						
2.5		ud		ud								